

## RESEARCH ARTICLE

# The *Trypanosoma brucei* subpellicular microtubule array is organized into functionally discrete subdomains defined by microtubule associated proteins

Amy N. Sinclair<sup>1</sup><sup>1</sup><sup>2</sup>, Christine T. Huynh<sup>1</sup><sup>1</sup>, Thomas E. Sladewski<sup>1</sup><sup>1</sup><sup>2</sup>, Jenna L. Zuromski<sup>2</sup><sup>2</sup>, Amanda E. Ruiz<sup>2</sup><sup>2</sup>, Christopher L. de Graffenried<sup>1</sup><sup>1</sup>\*

**1** Department of Molecular Microbiology and Immunology, Brown University, Providence, Rhode Island, United States of America, **2** Department of Pathology and Laboratory Medicine, Center for International Health Research, Brown University, Providence, Rhode Island, United States of America

<sup>1</sup><sup>2</sup> Current address: Department of Biology, Brandeis University, Waltham, Massachusetts, United States of America

<sup>2</sup><sup>2</sup> Current address: Department of Molecular and Cell Biology, University of Connecticut, Storrs, Connecticut, United States of America

\* [Christopher\\_degraffenried@Brown.edu](mailto:Christopher_degraffenried@Brown.edu)



## OPEN ACCESS

**Citation:** Sinclair AN, Huynh CT, Sladewski TE, Zuromski JL, Ruiz AE, de Graffenried CL (2021) The *Trypanosoma brucei* subpellicular microtubule array is organized into functionally discrete subdomains defined by microtubule associated proteins. *PLoS Pathog* 17(5): e1009588. <https://doi.org/10.1371/journal.ppat.1009588>

**Editor:** Kent L. Hill, University of California, Los Angeles, UNITED STATES

**Received:** November 11, 2020

**Accepted:** April 25, 2021

**Published:** May 19, 2021

**Copyright:** © 2021 Sinclair et al. This is an open access article distributed under the terms of the [Creative Commons Attribution License](https://creativecommons.org/licenses/by/4.0/), which permits unrestricted use, distribution, and reproduction in any medium, provided the original author and source are credited.

**Data Availability Statement:** All relevant data are within the manuscript and its [Supporting Information](#) files.

**Funding:** This study was funded by NIH NIAID R01 AI112953 (CLdG) and NIH NIAID F31 AI143163 (ANS). The funders had no role in study design, data collection and analysis, decision to publish, or preparation of the manuscript.

**Competing interests:** The authors have declared that no competing interests exist.

## Abstract

Microtubules are inherently dynamic cytoskeletal polymers whose length and organization can be altered to perform essential functions in eukaryotic cells, such as providing tracks for intracellular trafficking and forming the mitotic spindle. Microtubules can be bundled to create more stable structures that collectively propagate force, such as in the flagellar axoneme, which provides motility. The subpellicular microtubule array of the protist parasite *Trypanosoma brucei*, the causative agent of African sleeping sickness, is a remarkable example of a highly specialized microtubule bundle. It is comprised of a single layer of microtubules that are crosslinked to each other and to the overlying plasma membrane. The array microtubules appear to be highly stable and remain intact throughout the cell cycle, but very little is known about the pathways that tune microtubule properties in trypanosomatids. Here, we show that the subpellicular microtubule array is organized into subdomains that consist of differentially localized array-associated proteins at the array posterior, middle, and anterior. The array-associated protein PAVE1 stabilizes array microtubules at the cell posterior and is essential for maintaining its tapered shape. PAVE1 and the newly identified protein PAVE2 form a complex that binds directly to the microtubule lattice, demonstrating that they are a true kinetoplastid-specific MAP. TbAIR9, which localizes to the entirety of the subpellicular array, is necessary for maintaining the localization of array-associated proteins within their respective subdomains of the array. The arrangement of proteins within the array likely tunes the local properties of array microtubules and creates the asymmetric shape of the cell, which is essential for parasite viability.

## Author summary

Many parasitic protists use arrays of microtubules that contact the inner leaflet of the plasma membrane, typically known as subpellicular microtubule arrays, to shape their cells into forms that allow them to efficiently infect their hosts. While subpellicular arrays are found in a wide range of parasites, very little is known about how they are assembled and maintained. *Trypanosoma brucei*, which is the causative agent of human African trypanosomiasis, has an elaborate subpellicular array that produces the helical shape of the parasite, which is essential for its ability to move within crowded and viscous solutions. We have identified a series of proteins that have a range of localization patterns within the array, which suggests that the array is regulated by subdomains of array-associated proteins that likely tune the local properties of the microtubules to suit the stresses found at different parts of the cell body. These results establish a foundation to understand how trypanosomatid subpellicular arrays are built, shaped, and maintained, which has not previously been considered.

## Introduction

*Trypanosoma brucei* is the causative agent of African trypanosomiasis, which affects both humans and livestock in Sub-Saharan Africa [1]. A key contributor to *T. brucei* pathogenesis is the highly asymmetric shape of its cell body, which is essential for parasite survival within both insect and mammalian hosts. The trypomastigote form of *T. brucei* has a bore-like shape and tapered ends, with a broader cell posterior and a narrower, pointed anterior (Fig 1A). This shape is produced by a single layer of microtubules that underlies the plasma membrane called the subpellicular array [2,3]. A single flagellum is attached to the cell surface by the flagellum attachment zone (FAZ), which is comprised of a filament that is inserted between the subpellicular microtubules. The FAZ filament follows the left-handed helical path of the array microtubules as they traverse the cell body [4]. Flagellar beating deforms the subpellicular microtubule array and creates ‘cellular waveforms’ that define the distinctive corkscrew-like motility pattern of *T. brucei* [5–7]. This specialized motility is essential for parasite escape from high-flow blood vessels and capillaries into low-flow compartments, which leads to the invasion of epithelial and adipose tissues that facilitate persistent host infection and dissemination back to the insect vector [8–11]. The microtubules of the subpellicular array must be able to withstand and propagate the force generated by the flagellum, which is not uniformly distributed along the cell body [7]. The ability to regulate microtubule dynamics and flexibility within different domains of the array would allow the parasite to optimize the transmission of energy generated by the flagellar beat and channel it into productive motility.

Early morphological studies using electron microscopy revealed that the subpellicular array is a complex structure that is highly conserved among trypanosomatids [3,12]. The microtubules of the array are uniformly oriented, with their growing plus-ends facing the broader cell posterior [13–15]. The array microtubules are spaced apart at a consistent distance of 18–20 nm and are extensively crosslinked to each other and the plasma membrane by regularly spaced fibrils [16–18]. The widest point of the cell body, which is near the nucleus, can contain over 100 microtubules. As the cell tapers toward the posterior and anterior ends, microtubules terminate in a stepwise fashion that maintains the inter-microtubule distance and consistent spacing between crosslinking fibrils while creating the asymmetric shape of the trypanosome cell body [19].

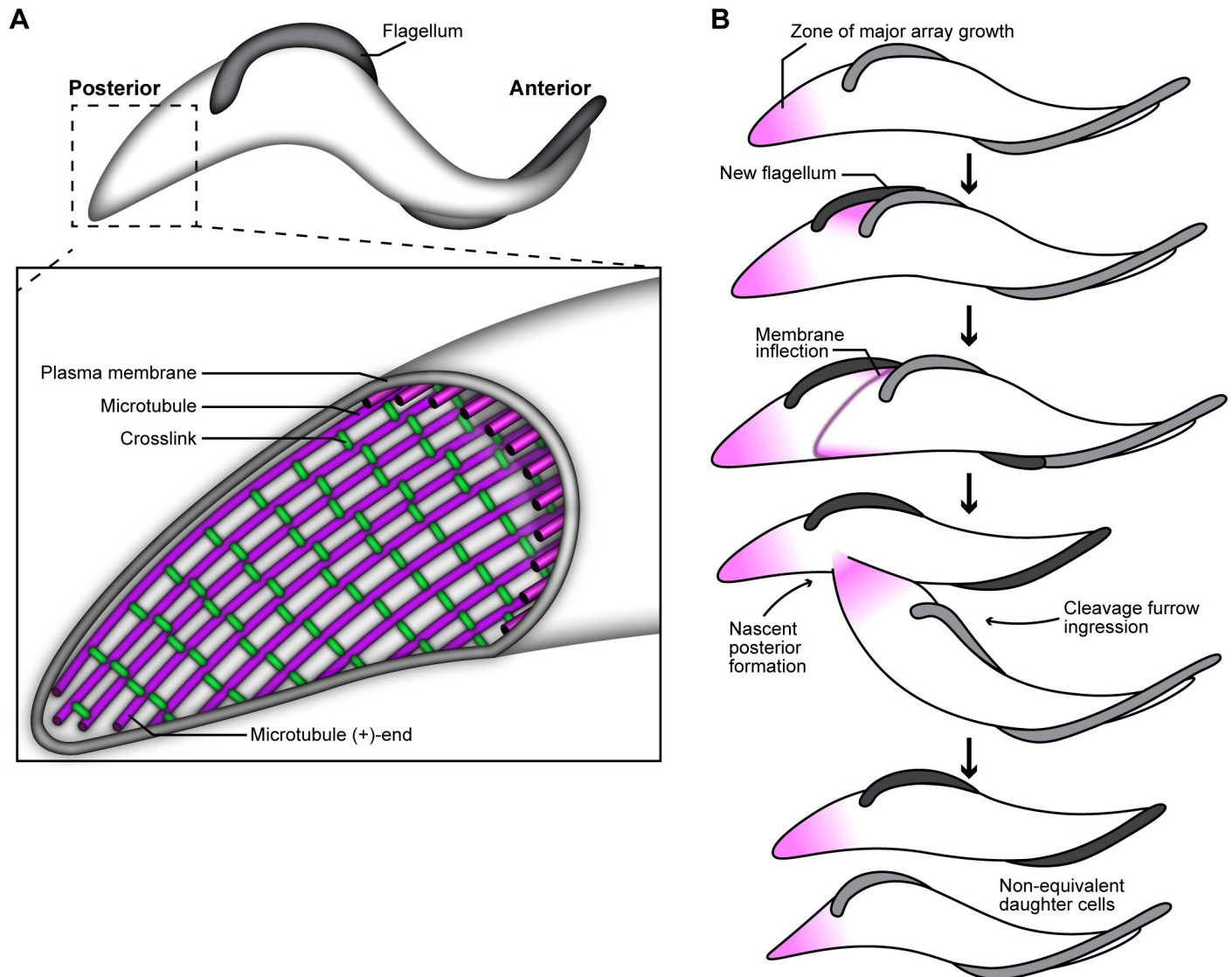


**Fig 1. Schematics of the cytoskeleton and cell division in *Trypanosoma brucei*.** (A) The subpellicular array is a single layer of microtubules (purple) that underlies the plasma membrane. The microtubules are crosslinked to each other by regularly spaced fibrils (green). The growing plus-ends of array microtubules face the cell posterior. (B) Array microtubules appear to consistently polymerize at the posterior end of the cell (purple shading). As the new flagellum is nucleated, new microtubules are inserted between the old and new flagellum to increase cell width. A membrane inflection forms that demarcates the path of cleavage furrow ingression, which follows the helical path of array microtubules. Cleavage furrow ingression initiates at the cell anterior, and nascent posterior end formation remodels the array at the cell midzone to resolve the subpellicular array into two distinct structures to complete cytokinesis.

<https://doi.org/10.1371/journal.ppat.1009588.g001>

Microtubules are rigid, hollow polymers made up of  $\alpha$ - and  $\beta$ -tubulin heterodimer subunits that bind and hydrolyze GTP. They exhibit a property known as dynamic instability wherein they undergo GTPase-dependent cycles of depolymerization ('catastrophes') and growth ('rescues') [20]. This property allows for the rapid reorganization of internal cytoskeletal networks and is essential for cell migration, intracellular transport, and division [21]. Microtubules are organized and regulated by microtubule associated proteins (MAPs) and motor proteins such as kinesins to control their dynamic instability. Many MAPs crosslink microtubules into bundles that can propagate and withstand force, such as the bundles found at the mitotic spindle, ciliary axoneme, and neuronal axon [22–25]. Tubulin subunits have intrinsically disordered and highly charged C-terminal tails that are heavily decorated with post-translational

modifications, which serve as binding sites for many MAPs [26,27]. Other MAPs recognize specific structural conformations of the microtubule lattice, such as the incompletely polymerized and more open lattice found at growing microtubule plus-ends [28,29]

The subpellicular microtubule array of *T. brucei* is a fascinating example of a specialized microtubule bundle. Dynamic instability has not been observed in microtubules of the array, most likely due to their extensive crosslinking (Fig 1A). Some crosslinking proteins in other systems are known to promote microtubule flexibility [30], which may explain the apparent longevity of subpellicular array microtubules as they respond to forces produced by the flagellar beat. However, very little is known about the structure and function of the inter-microtubule crosslinking fibrils that organize the array or how MAPs may regulate array microtubules. Fewer than twenty non-motor proteins have been identified that associate with the subpellicular array [31]. The function of many of these has yet to be determined, but a subset have been described as microtubule stabilizers or potential crosslinkers that are required for proper cell division [32–35] and the arrangement of array microtubules in a single layer underneath the plasma membrane [36–38]. However, the precise mechanisms these proteins employ to localize to the array and perform their function have not been established. Understanding how *T. brucei* MAPs bind to microtubules will have important implications in trypanosomatid cell biology and provide a more fundamental understanding of how cytoskeletal filaments are organized among diverse phyla.

The array microtubules appear highly stable and remain intact throughout the cell cycle, which requires that many aspects of *T. brucei* cell division include microtubule remodeling processes that duplicate and segregate the array (Fig 1B) [13,39]. During cell division, extant microtubules are elongated and short, new microtubules are inserted between them to lengthen and widen the array [16]. At later stages of the cell cycle, new microtubules are inserted between the old and new flagellum to widen the cell body [40]. Microtubule polymerization also appears to occur continuously at the cell posterior throughout the cell cycle, suggesting that the array microtubules may be consistently turning over tubulin subunits to maintain cell length and shape [14,40,41]. Cytokinesis proceeds via a cleavage furrow that initiates at the cell anterior and follows the helical path of the array microtubules towards the cell posterior to divide the cell on its long axis (Fig 1B) [13,16,42].

Very little is known about how the subpellicular microtubule array is constructed and how it maintains its shape throughout the lifetime of the cell. In this work, we show that the subpellicular array contains a landscape of differentially localized array-associated proteins that likely function to locally tune the biophysical characteristics of array microtubules. These array-associated proteins play important roles in maintaining cell shape and create discrete subdomains within the array. We define the function of an array-associated protein known as PAVE1, which is found exclusively in kinetoplastids and localizes to the posterior subdomain of the array [43]. We previously showed that PAVE1 is an essential protein that is required for cell division and the formation of the tapered cell posterior. We now show that PAVE1 localizes to the microtubules of the posterior subpellicular array and may be a component of the inter-microtubule crosslinking fibrils present in the posterior subdomain. We also find that PAVE1 is essential for stabilizing the growing microtubules found within this subdomain. PAVE1, in complex with its binding partner PAVE2, binds directly to the microtubule lattice in vitro, demonstrating that PAVE1 and PAVE2 together form a true kinetoplastid-specific MAP. The previously identified protein TbAIR9 [35] forms a complex with PAVE1 and PAVE2 and maintains the distribution of array-associated proteins at their specific subdomains within the subpellicular array. These results update the long-standing view of the subpellicular array as a static arrangement of microtubules. We show that the array is a dynamic, multidomain structure that plays an essential role in cell morphogenesis and motility.

## Results

### PAVE1 localizes to microtubules of the subpellicular array at the cell posterior

PAVE1 (Posterior And Ventral Edge protein 1) is an array-associated protein that localizes to the posterior and ventral edge of the subpellicular array [43]. To determine if PAVE1 localizes to regions of new microtubule growth, we compared PAVE1 distribution to the labelling pattern of the antibody YL1/2, which recognizes the terminal tyrosine residue of  $\alpha$ -tubulin [44]. Terminal tyrosination is a hallmark of newly polymerized tubulin and is considered a marker of array growth during the cell cycle [16,40,45]. We generated a cell line that contained PAVE1 endogenously tagged with three copies of the Ty1-epitope tag at its N-terminus, fixed the cells using methanol, and stained them with anti-Ty1 and YL1/2 antibodies to examine their distribution throughout the cell cycle (Fig 2A). Trypanosomes contain one nucleus (N) and one kinetoplast (K; the mitochondrial DNA aggregate) early in the cell cycle (1N1K). Cells first duplicate their kinetoplast (1N2K) before undergoing karyokinesis (2N2K) prior to initiating cytokinesis. Ty1-PAVE1 and YL1/2 both stain the posterior array of cells early in the cell cycle (1N1K) with the labeling density declining as the array widens near the location of the kinetoplast (Fig 2A, asterisk). YL1/2 also labels a pool of tyrosinated tubulin present at the basal body (Fig 2A, open arrowheads) [46]. In late 1N1K cells, which can be identified by their elongated kinetoplasts, the YL1/2 signal declines at the cell posterior while PAVE1 signal remains unchanged. In 1N2K cells, YL1/2 signal increases and becomes more concentrated at the cell posterior, indicating more localized array growth, with no change in PAVE1 labeling pattern. In 2N2K cells, the PAVE1 signal extends past the midzone of the cell towards the more anterior-located nucleus, which is the location of extensive microtubule remodeling that leads to the creation of the new posterior end during cytokinesis [40]. This localization pattern suggests that PAVE1 is stably associated with the array at the posterior end of the cell throughout the cell cycle and is recruited to the nascent posterior end during its formation.

PAVE1 may localize to specific regions of individual microtubules in the subpellicular array to carry out its function. We performed negative-stain immunogold electron microscopy (iEM) on whole-mount extracted cytoskeletons prepared from cells containing Ty1-tagged PAVE1 to obtain high-resolution localization information (S1A Fig). The 20 nm gold particles labeling Ty1-PAVE1 localized to the posterior portion of the subpellicular array with very little labeling on the cell anterior. However, it was not possible to determine if PAVE1 preferentially bound a specific region of individual microtubules. When whole-mount cytoskeletons are imaged by TEM, both the top and bottom layers of the array are visible, which results in a cross-hatching pattern that makes it difficult to distinguish individual microtubules. To address this problem, we generated subpellicular array sheets from immunogold-labeled cytoskeletons [16]. Extracted whole-mount immunogold-labeled cytoskeletons were positively stained with uranyl acetate, critical point dried, and cleaved using double-sided tape to 'unroof' the cell and remove the top layer of the subpellicular array (Fig 2B).

To determine if PAVE1 has a restricted labeling pattern along individual microtubules, we compared PAVE1 distribution to the localization pattern of the TAT1 antibody, which recognizes *T. brucei*  $\alpha$ -tubulin (Fig 2B, left) [47]. We developed a semi-automated macro in ImageJ [48] that allowed us to quantify the localization of immunogold labeling (S1B Fig). Subpellicular sheets were oriented along their dorsal-ventral axis using the intact flagellum as a fiducial marker. Gold beads were then classified as localizing to the dorsal, centroid, or ventral regions of individual array microtubules. We found that in comparison to TAT1 labeling, PAVE1 preferentially localized to the outside ventral walls of the array microtubules at the cell posterior, as well as to the inter-microtubule crosslinks that remained after sheet preparation (Fig 2C and

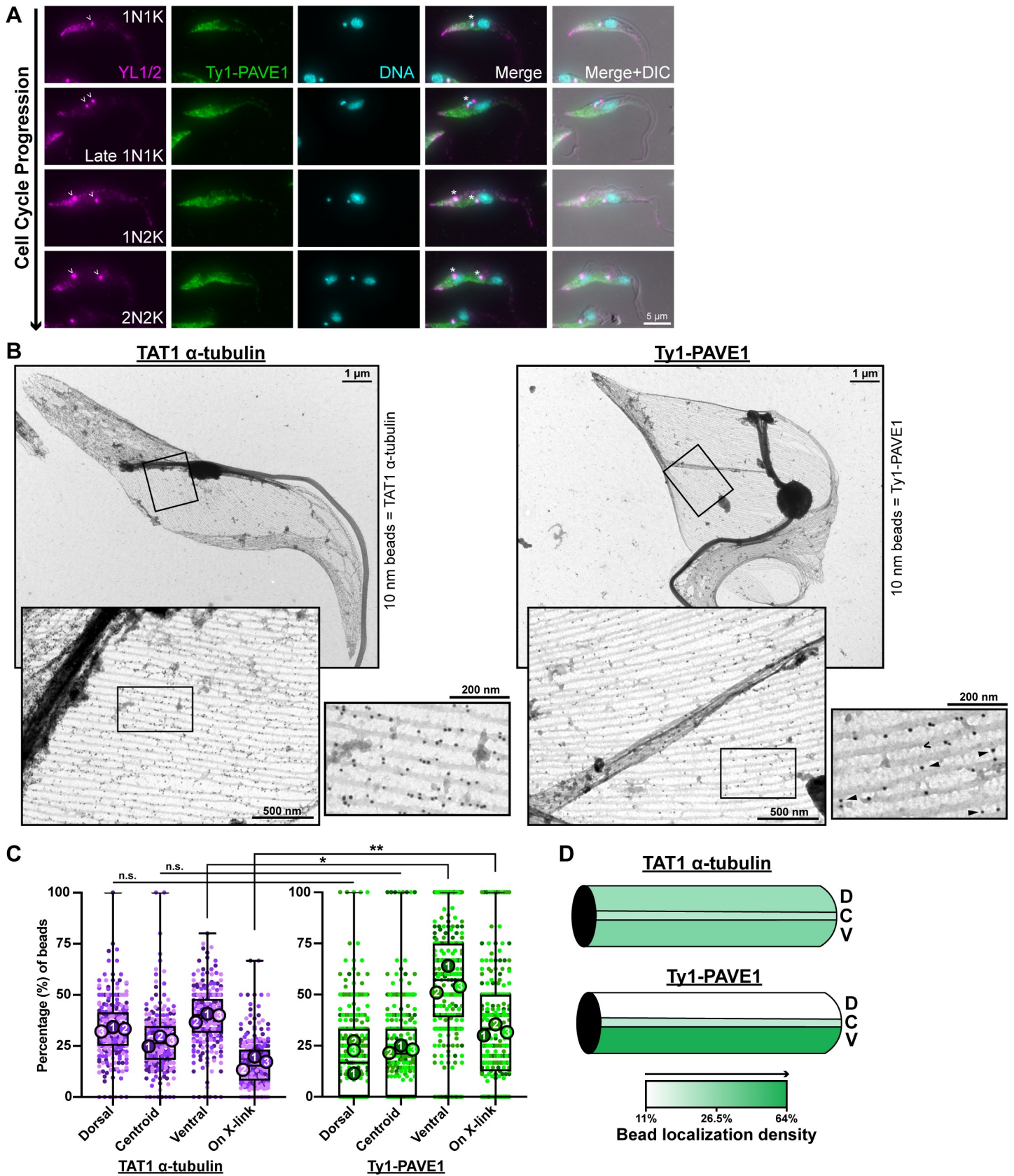


**Fig 2. PAVE1 localizes to the subpellicular array microtubules of the cell posterior.** (A) Ty1-PAVE1 cells were fixed in methanol and labeled with anti-Ty1 antibody and YL1/2, which recognizes tyrosinated tubulin. The empty arrowheads are denoting pools of tyrosinated  $\alpha$ -tubulin at the basal body. Asterisks are marking kinetoplasts. (B) (Left) A subpellicular array sheet from WT 427 control cells immunogold-labeled with 10 nm beads using TAT1 antibody, which recognizes trypanosome  $\alpha$ -tubulin. (Right) A subpellicular array sheet immunogold-labeled for Ty1-PAVE1 with 10 nm beads. Empty arrowhead is pointing to the ventral protrusion of a disrupted crosslink, and solid arrows are marking Ty1-PAVE1 beads on preserved inter-microtubule crosslinking fibrils. (C) Quantification of immunogold label distribution along individual microtubules in subpellicular sheets represented as a Superplot [89], which shows each individual measurement in each biological replicate. The replicates are color-coded and the average is illustrated as large circles. TAT1  $\alpha$ -tubulin—Ty1-PAVE1 dorsal:dorsal and centroid:centroid distributions are not significantly different ( $P = 0.0542$  and  $P = 0.0741$ , respectively). \* $P = 0.0146$ , \*\* $P = 0.0032$ . P-values are calculated from unpaired two-tailed Student's *t*-tests using the averages from  $N = 3$  independent biological replicates. 3 subpellicular sheets in both TAT1 control and Ty1-PAVE1 conditions from  $N = 3$  independent biological replicates were quantified. (D) Heat map of  $\alpha$ -tubulin and Ty1-PAVE1 immunogold label distribution on individual microtubules. Shading is representative of the average distribution of labeling from (C). D; dorsal, C; centroid, V; ventral.

<https://doi.org/10.1371/journal.ppat.1009588.g002>

2D). Many crosslinks were disrupted in the sheet preparation, leaving small protrusions on the outside microtubule wall (Fig 2B, open arrowhead). The ventral localizations of PAVE1 often occurred on these protrusions, indicating that PAVE1 may localize to a disrupted crosslink. It is important to note that the two-stage antibody label employed to detect PAVE1 creates uncertainty in the precise location of the protein due to the additional distance introduced between the antigen and the gold particles used for detection, which limits our ability to precisely localize PAVE1 [49]. However, the significant difference in the distribution pattern of TAT1 and Ty1-PAVE1 gold particles is suggestive of PAVE1 interacting with the crosslinking fibrils of the posterior array (Fig 2C).

### PAVE1 maintains microtubule length at the posterior subpellicular array

While new tubulin dimers are added to the microtubule plus-ends present at the cell posterior throughout the cell cycle, new microtubules are intercalated into the array between existing microtubules during cell division to enlarge the cell circumference [16,40]. It is not known how array-associated proteins or microtubule crosslinking fibrils are incorporated into the array. To determine how PAVE1 is incorporated into the array, we developed a capping assay using HaloTag technology, which irreversibly conjugates a dye to a specific fusion protein [50]. We appended the HaloTag protein to the N-terminus of one of the endogenous PAVE1 alleles, then incubated an exponentially growing culture with a cell-permeable HaloTag substrate containing the far-red fluor JF646 to covalently label all the extant HaloTag-PAVE1 present in the cell. The remaining JF646-conjugated substrate was then washed out of the culture and replaced with a substrate linked to the rhodamine analog TMR, which is only able to label newly synthesized HaloTag-PAVE1 (Fig 3A). Cells were then harvested, fixed, and imaged using epifluorescence microscopy. The fluorescence intensity of each fluor-conjugated version of PAVE1 was analyzed using a line scan placed along the ventral edge of the cell body of 1N1K cells (Fig 3B and 3C). This two-color labeling approach allowed us to localize where newly synthesized PAVE1 was added to the array and how the distribution of PAVE1 at steady state changed over time. We designated  $T = 0$  h as the point when the TMR substrate was added to the media for our subsequent analysis.

At  $T = 0$  h, the JF646 signal labeled the posterior and ventral edge of cells in a similar pattern to what was observed with Ty1-PAVE1 immunofluorescence. There was an additional punctum of JF646 and TMR signal near the endomembrane system (Fig 3A, asterisk), which was likely due to endocytosis of the HaloTag substrate. At  $T = 1$  h, the TMR signal was greatest at the extreme posterior end of the cell and rapidly declined towards the cell anterior (Fig 3B). This suggested that new HaloTag-PAVE1 was added to the extreme posterior of the subpellicular array at the same location that microtubule polymerization occurs throughout the cell cycle. At  $T = 3$  h, the TMR signal began to increase past the extreme posterior end. This demonstrated that HaloTag-PAVE1 moved toward the cell anterior as newly synthesized PAVE1

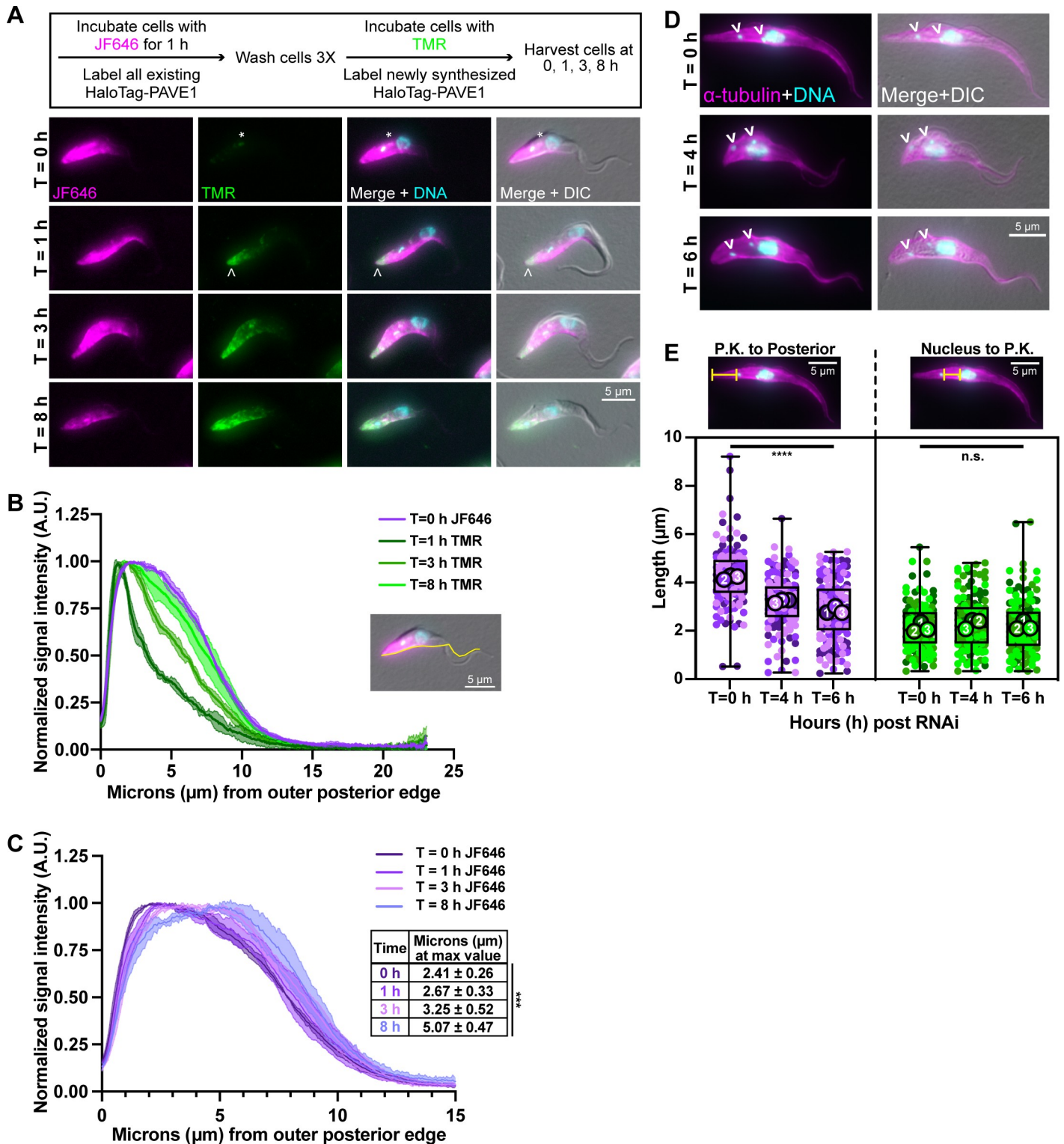


**Fig 3. PAVE1 is added to and stabilizes the microtubules at the extreme posterior end of the array.** (A) HaloTag-PAVE1 cells were fixed in paraformaldehyde at T = 0 h, T = 1 h, T = 3 h, and T = 8 h after the addition of TMR-conjugated HaloTag ligand to cell culture in the capping assay. Asterisk represents background labeling of the endomembrane system. Empty arrowhead is pointing to the earliest addition of HaloTag-PAVE1, represented by TMR labeling, at the extreme cell posterior. (B) Fluorescence intensity quantification of HaloTag ligand labeling along the ventral edge of the cell body at T = 0 h, T = 1 h, T = 3 h, and T = 8 h after TMR substrate addition. Fluorescence intensity was normalized to 1 at each time point in order to illustrate the shape of the curve. 50 1N1K cells at each time point from N = 3 independent biological replicates were measured. (C) Fluorescence intensity quantification of JF646-HaloTag ligand labeling as in (B). Inset displays the distance

in  $\mu\text{m}$  at which the maximum intensity of JF646 ligand was located. 50 1N1K cells at each time point from  $N = 3$  independent biological replicates were measured. One-way ANOVA was calculated using the averages from  $N = 3$  independent biological replicates.  $***P < 0.001$ . (D) PAVE1 RNAi was induced and cells were harvested, fixed in methanol, and stained with anti- $\alpha$ -tubulin after  $T = 0$  h,  $T = 4$  h, and  $T = 6$  h of PAVE1 RNAi induction. 1N2K cells were selected for analysis as they completed cytokinesis prior to PAVE1 depletion. (E) Superplot of the measured distances between the posterior kinetoplast to outer posterior edge of the subpellicular array, and the posterior edge of the nucleus to the posterior kinetoplast in control and PAVE1 RNAi cells. 50 1N2K cells were measured at each time point from  $N = 3$  independent biological replicates. One-way ANOVAs were calculated using the averages from each replicate.  $****P < 0.0001$ , n.s.  $P = 0.5653$ .

<https://doi.org/10.1371/journal.ppat.1009588.g003>

protein is incorporated into the array. At the latest time point  $T = 8$  h, which was approximately the duration of one cell cycle, the TMR signal pattern was similar to the original JF646 signal. The JF646 signal intensity declined at  $T = 8$  h while the TMR signal intensity increased, which suggests that there is turnover of HaloTag-PAVE1 on the array as it migrates towards the cell anterior. Consistent with this observation, the signal maxima of JF646-labeled HaloTag-PAVE1, which is representative of steady-state PAVE1 localization, also moved toward the cell anterior over time (Fig 3C).

Depletion of PAVE1 using RNA interference (RNAi) truncates the subpellicular array until the posterior cell edge abuts the kinetoplast [43]. We performed an RNAi time course to test if PAVE1 is required to maintain the microtubules of the posterior array, or if the array truncation seen in PAVE1-depleted cells is the result of aberrant cell division. Considering that cultured *T. brucei* cells are asynchronous and that there are currently no established methods for synchronizing these cells that are compatible with RNAi, we developed a strategy to identify cells that had completed cell division prior to PAVE1 RNAi induction. We induced PAVE1 RNAi in log-phase cell cultures and harvested cells after 4 or 6 h of RNAi induction and restricted our analysis to 1N2K cells to select for cells that had progressed well into G1 phase at the time of PAVE1 depletion. The cell cycle for the 29.13 line carrying the PAVE1 RNAi hairpin is 12.9 h. Previous studies have shown that 1N2K cells would have initiated cell division approximately 10.8 h (0.84 units) prior to the time of harvest [39]. Selecting 1N2K cells allowed us to eliminate any confounding effects on array morphology from cytokinesis and the posterior end remodeling that occurs in G1 phase immediately following cytokinesis, as these cells will have already completed these processes prior to PAVE1 RNAi induction [40,41]. Thus, any defects observed in the array of 1N2K cells would be the direct result PAVE1 depletion (Fig 3D).

We visualized the array microtubules using immunofluorescence microscopy with an anti- $\alpha$ -tubulin antibody and measured the length of the array from the more posterior kinetoplast to the posterior edge of the cell in PAVE1 RNAi and control 1N2K cells. We found that the posterior array of PAVE1 RNAi cells at  $T = 4$  h were significantly shorter than  $T = 0$  h cells by an average of  $0.99 \pm 0.12 \mu\text{m}$  (Fig 3E). Moreover, the average posterior array length of PAVE1 RNAi cells at  $T = 6$  h was  $1.38 \pm 0.23 \mu\text{m}$  shorter than  $T = 0$  h cells. However, the length of the array between the nucleus and posterior kinetoplast was the same at all three time points, which indicates that PAVE1 RNAi did not cause repositioning of the kinetoplast within the cell body or a shortening of the array at the cell midzone. These data suggest that PAVE1 is required to maintain the extended, tapering portion of microtubules at the cell posterior independent of its potential function during formation of the nascent cell posterior during cell division.

### PAVE1 immunoprecipitation reveals two potential interacting partners

Considering the localization pattern of PAVE1 on the subpellicular microtubules, it is possible that PAVE1 is part of a protein complex that forms the inter-microtubule crosslinks or interacts with other MAPs within this part of the array. To identify other proteins that may interact

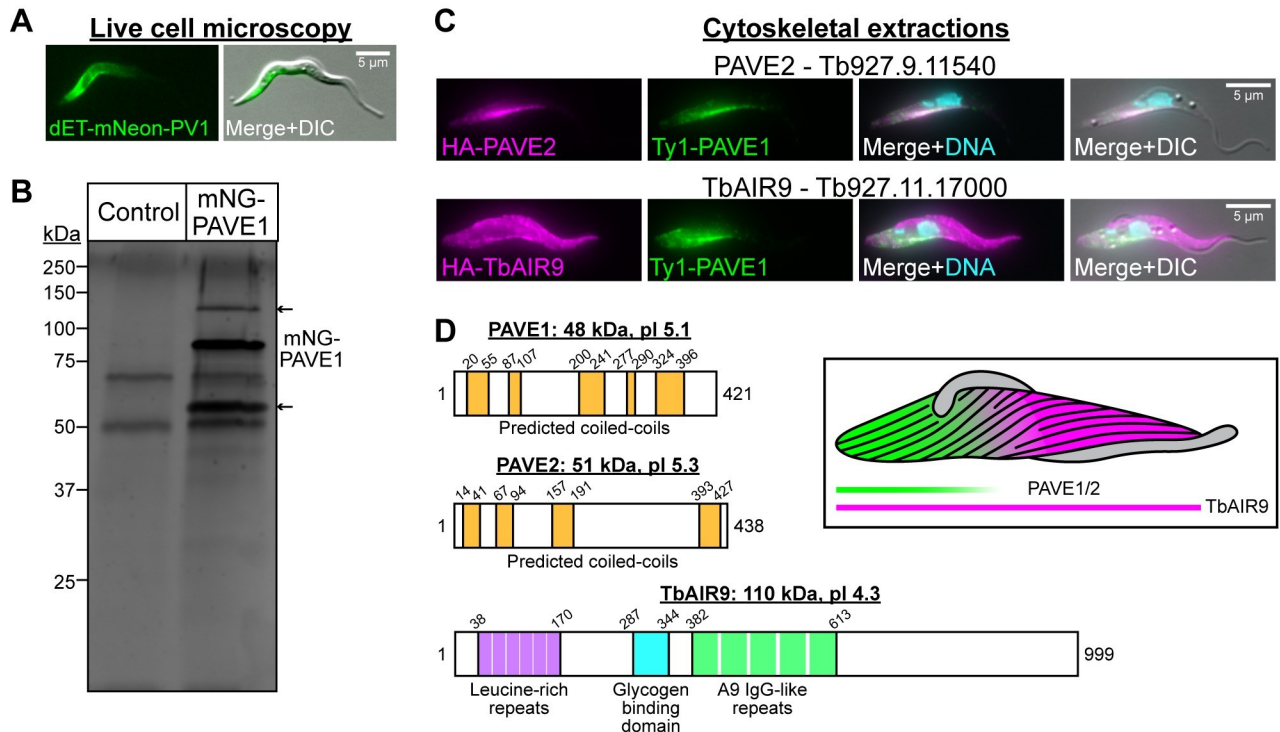


**Fig 4. Immunoprecipitation of mNeonGreen-PAVE1 reveals two interacting partners.** (A) Representative image of a live *T. brucei* cells expressing mNeonGreen-PAVE1 from both endogenous loci. (B) dET-mNeonGreen-PAVE1 cells were harvested, lysed, and sonicated to solubilize cytoskeletal proteins. Clarified supernatant was batch-bound with magnetic camelid nanobodies against mNeonGreen. Beads were washed 6X and bound proteins were analyzed by mass spectrometry. Gel is a representative silver-stained SDS-PAGE gel of the elution from the mNeonGreen immunoprecipitation in control and mNeonGreen-PAVE1 samples. Both lanes are 50% of input material. Arrows indicate the two major unique protein bands present in the mNeonGreen-PAVE1 sample not present in WT 427 controls. (C) The two potential interacting partners of PAVE1 identified in the mNeonGreen-PAVE1 immunoprecipitation were endogenously tagged with the HA epitope tag. The cytoskeleton was extracted and cells were processed for immunofluorescence to co-localize each protein with Ty1-PAVE1 using anti-Ty1 and anti-HA antibody. (D) Protein domain schematics including the predicted molecular weight (kDa) and pI for PAVE1, PAVE2, and TbAIR9. PAVE1 and PAVE2 have no recognizable domain homology to any known protein. However, they contain a series of predicted coiled coils [58]. TbAIR9 lacks the basic serine-rich microtubule binding site found in *Arabidopsis thaliana* AIR9, but does contain the conserved leucine-rich repeats, glycogen binding domain, and A9 IgG-like folds. Inset illustrates the localization pattern of PAVE1, PAVE2, and TbAIR9 across the array.

<https://doi.org/10.1371/journal.ppat.1009588.g004>

with PAVE1, we endogenously tagged both PAVE1 alleles with the fluorescent protein mNeonGreen (mNG) at their N-termini (Fig 4A) and immunoprecipitated mNG-PAVE1 using mNeonGreenTrap antibody. Fractions of the eluate examined by SDS-PAGE and subsequent silver staining showed two primary unique bands compared to the control eluate (Fig 4B). Mass spectrometry analysis of on-bead tryptic digests generated from mNG-PAVE1 and control immunoprecipitations revealed two potential interacting partners whose predicted molecular weight matched that of the unique bands on the silver-stained gel (S1 Table). These potential interactors were an uncharacterized protein (Tb927.9.11540, predicted MW 51 kDa) and TbAIR9 (Tb927.11.17000, predicted MW 110 kDa).

We appended triple-HA epitope tags to the N-termini of the potential interactors in a cell line already harboring Ty1-tagged PAVE1, then performed cytoskeletal extractions followed by immunofluorescence microscopy. The uncharacterized HA-tagged protein Tb927.9.11540 was stably associated with the cytoskeleton and co-localized with Ty1-PAVE1, so we termed this new protein PAVE2 (Fig 4C, top). HA-TbAIR9 was stably associated with the entire array, as previously reported [35]. There was more intense staining of HA-TbAIR9 at the anterior portion of the array, where the Ty1-PAVE1 signal is minimal (Fig 4C, bottom).

### PAVE1 and PAVE2 require each other for stability and localization

Like PAVE1, PAVE2 is conserved in kinetoplastids and lacks homologs in other domains of life. Domain detection and structure prediction programs [51–57] did not identify known microtubule-interacting domains or any other potential motifs in either PAVE1 or PAVE2 (Fig 4D), but both proteins are predicted to contain coiled coil secondary structure [58]. PAVE2 was previously identified as a potential interactor of the cytokinetic regulator TOE-FAZ1 in the same proximity-dependent biotin identification screen that originally identified PAVE1 [43]. To test its function, we conducted RNAi against PAVE2 and found that cells were unable to divide after 4 d of RNAi induction (S2A and S2B Fig). After 2 d of PAVE2 RNAi, there was an accumulation of multinucleated cells (MultiN), cells with two nuclei and one kinetoplast (2N1K), and anucleate zoids (0N1K) (Fig 5A and 5B), which is similar to the cell division defect observed in PAVE1 RNAi [43]. These aberrant cell types significantly increased in proportion after 4 d of PAVE2 depletion.

Strikingly, we saw that PAVE2 depletion resulted in cell bodies whose posterior ends abutted the kinetoplast (Fig 5A, empty arrowheads), which mirrors the PAVE1 RNAi posterior truncation phenotype [43]. The microtubules of truncated posterior arrays in PAVE2 RNAi cells were also disorganized in comparison to control cells when analyzed by whole-mount TEM (Fig 5C). We measured the length of the posterior array in control and PAVE2 RNAi cells to confirm the truncation phenotype. We found that the mean distance between the kinetoplast and posterior end of 1N1K cells was an average of  $1.62 \pm 0.31 \mu\text{m}$  shorter than controls after 24 h of RNAi induction, while the distance between the nucleus and kinetoplast remained constant (Fig 5D). This suggested the posterior truncation phenotype was not due to aberrant kinetoplast placement or defects in the array at other locations but to the specific destabilization of microtubules at the posterior array, which phenocopies PAVE1 RNAi.

Both PAVE1 and PAVE2 RNAi result in the truncation of the posterior array, which suggests that these proteins may have a shared function or may form a complex. We depleted PAVE1 and determined the localization of PAVE2 to establish if PAVE2 relied on PAVE1 for localization or stability within the cell. We found that HA-tagged PAVE2 localization to the posterior subpellicular array decreased as Ty1-PAVE1 protein levels declined (Fig 5E). Western blot analysis showed that PAVE2 protein levels also decreased during PAVE1 RNAi (S2C Fig). We found that the inverse relationship existed as well; when PAVE2 was depleted by RNAi, PAVE1 did not localize to the posterior array (Fig 5F) and its levels were reduced (S2D Fig). These results suggest that PAVE1 and PAVE2 require each other for localization and stability inside the cell.

### PAVE1 and PAVE2 form a microtubule-associated complex *in vitro*

The interdependence of PAVE1 and PAVE2 *in vivo* (Fig 5) and their near 1:1 stoichiometry in the PAVE1 immunoprecipitation (Fig 4B) suggest that these two proteins may form a complex. To test this, we co-expressed PAVE1 and PAVE2 recombinantly in *Escherichia coli*. The solubility-promoting maltose binding protein (MBP) followed by an oligo-His<sub>10</sub> tag and TEV protease site were appended to the N-terminus of mNG-PAVE1, while a Strep peptide tag was added to the N-terminus of PAVE2. Lysates from *E. coli* co-expressors were incubated with nickel resin, followed by elution of the captured proteins and treatment with TEV protease to cleave the MBP-oligoHis<sub>10</sub> tag from mNG-PAVE1. Subsequent capture of the eluate with Strep-Tactin resin resulted in a pure complex of mNG-PAVE1 and Strep-PAVE2, which we termed the PAVE complex (Fig 6A, left). Attempts to purify either PAVE1 or PAVE2 on their own were not successful, which suggests that these proteins require each other for proper folding. The purified PAVE complex was diluted into a low salt buffer and then clarified by

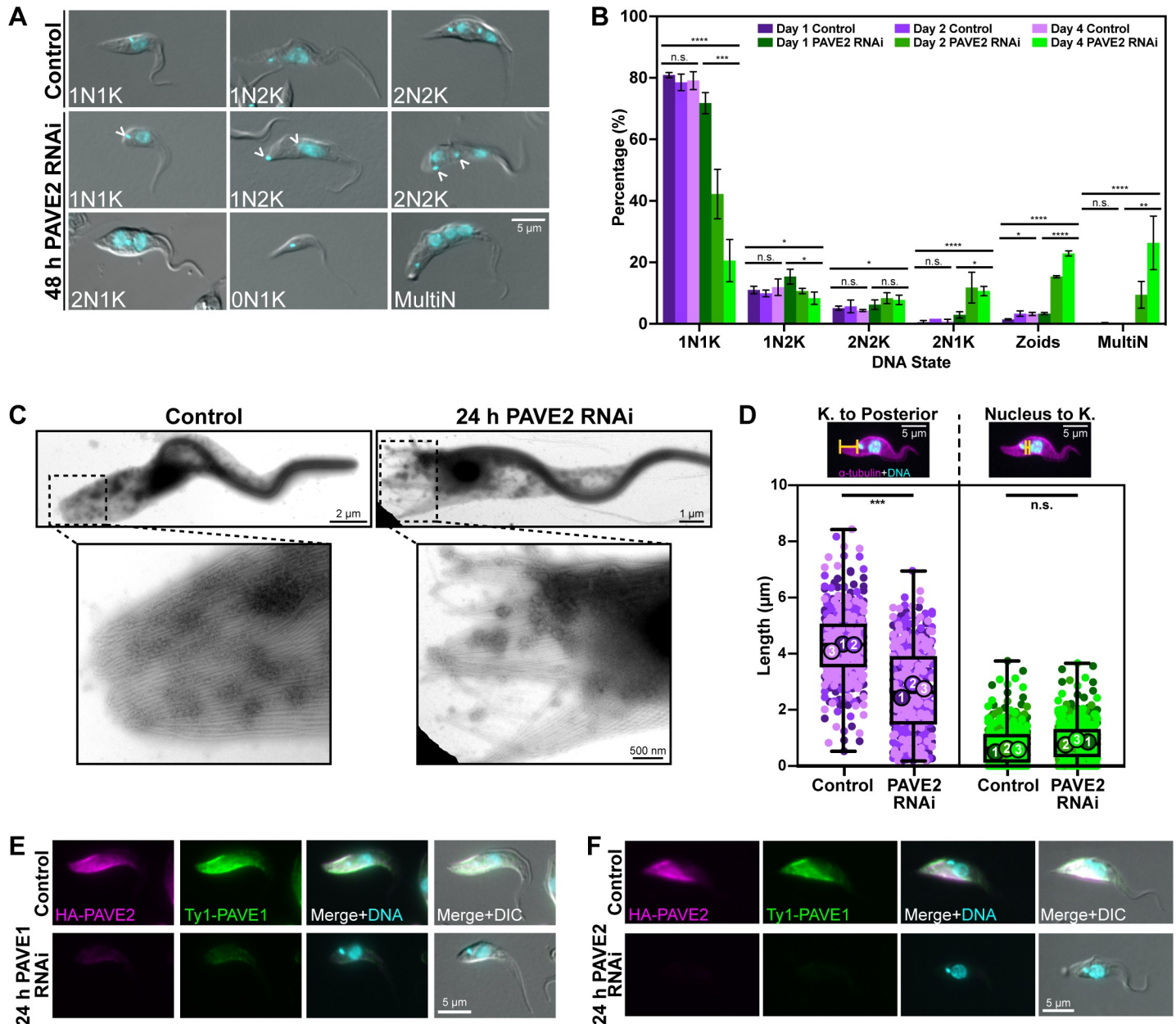


**Fig 5. PAVE2 phenocopies PAVE1.** (A) PAVE2 RNAi was induced for 2 d, after which control and PAVE2-depleted cells were fixed with paraformaldehyde and examined by epifluorescent microscopy. (B) Quantification of DNA states in control and PAVE2 RNAi cells after 1, 2, and 4 d of RNAi induction. Bars represent the mean and the error bars are the S.D. 300 cells in both control and PAVE2 RNAi conditions from N = 3 independent biological replicates were counted at each time point. One-way ANOVAs were calculated using the averages from each replicate. \*\*\*\* $P < 0.0001$ , \*\*\* $P < 0.0005$ , \*\* $P < 0.005$ , \* $P < 0.05$ , n.s.  $P > 0.05$ . (C) Whole-mount transmission electron microscopy of control and PAVE2 RNAi cells after 1 d of PAVE2 depletion. (D) PAVE2 RNAi was induced for 1 d and cells were harvested, fixed in paraformaldehyde, and stained with anti- $\alpha$ -tubulin to demarcate the subpellicular array. Superplot is of the measured distance between the kinetoplast and the outer posterior edge of the array, and the posterior edge of the nucleus to the kinetoplast of 1N1K cells in control and PAVE2 RNAi conditions. 100 1N1K cells were measured for both control and PAVE2 RNAi conditions in N = 3 independent biological replicates. Unpaired two-tailed Student's *t*-tests were performed using the averages from N = 3 independent biological replicates. \*\*\* $P = 0.0006$ . n.s.  $P = 0.0753$ . (E) Control and PAVE1 RNAi cells were fixed in paraformaldehyde and stained after 1 d of PAVE1 depletion. PAVE2 does not localize to the array in the absence of PAVE1. (F) Control and PAVE2 RNAi cells were fixed in paraformaldehyde and stained after 1 d of PAVE2 depletion. PAVE1 does not localize to the array in the absence of PAVE2.

<https://doi.org/10.1371/journal.ppat.1009588.g005>

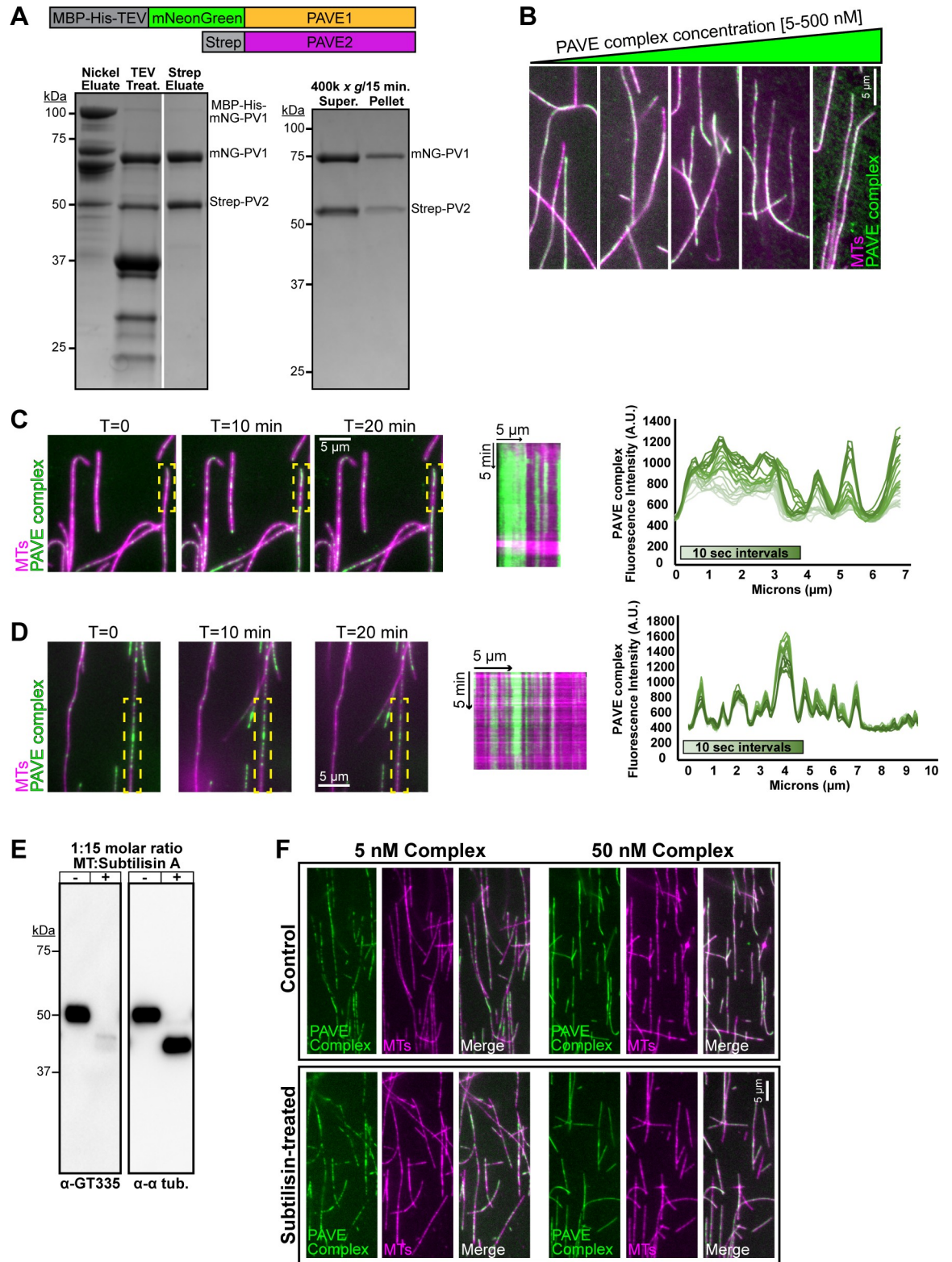


**Fig 6. PAVE1 and PAVE2 form a complex in vitro that binds the microtubule lattice.** (A) (Left) Coomassie-stained SDS-PAGE gel demonstrating the co-purification of mNeonGreen-PAVE1 and Strep-PAVE2 from *E. coli* cells. *E. coli* cells co-expressing [MBP-oligoHis<sub>10</sub>-TEV]-mNeonGreen-PAVE1 and Strep-PAVE2 constructs were harvested, lysed, and the clarified supernatant was batch-bound with Ni-NTA resin. The eluate was treated with TEV protease and allowed to interact with Strep-Tactin XT resin. Proteins were

eluted using 50 mM biotin. The Strep eluate lane contains 4  $\mu$ g of protein. (Right) The PAVE complex was diluted into a low salt buffer containing 50 mM NaCl and ultracentrifuged. Equal fractions of both the supernatant and pellet were separated on an SDS-PAGE gel and stained with Coomassie blue. (B) 5, 50, 100, 200, and 500 nM clarified PAVE complex was incubated with Taxol-stabilized bovine microtubules labeled with the Cy5 fluor for 20 min RT. The PAVE complex-microtubule solution was settled onto a blocked flow cell and unbound protein was washed away. The flow cell was imaged using epifluorescence microscopy. (C) (Left) A PEGylated flow cell was blocked and Taxol-stabilized bovine Cy5-microtubules were allowed to attach to the flow cell surface. 5 nM clarified PAVE complex was added to the flow cell chamber and immediately imaged using TIRF microscopy. Images were taken every 10 sec for 20 min. (Middle) Kymograph of PAVE complex on the microtubule outlined in yellow. (Right) Fluorescence intensity line scan of the microtubule outlined in yellow for the first 4 min 10 sec of TIRF imaging. (D) (Left) 5 nM clarified PAVE complex was mixed with Taxol-stabilized bovine Cy5-microtubules for 10 min RT to pre-seed patches. The PAVE complex-microtubule mixture was flowed into a blocked and PEGylated flow cell and allowed to attach to the flow cell surface. Unbound protein was washed away and the flow cell was immediately imaged using TIRF microscopy. Images were taken every 10 sec for 20 min. (Middle) Kymograph of PAVE complex on the microtubule outlined in yellow. (Right) Fluorescence intensity line scan of the microtubule outlined in yellow for the first 4 min 10 sec of TIRF imaging. (E) Control microtubules and microtubules treated with subtilisin A were collected for western blotting. The post-translational modification of glutamylation is no longer present on subtilisin-treated microtubules, as detected with the antibody GT335, and there is a molecular weight shift showing that the C-terminal tails have been cleaved, as detected with anti- $\alpha$ -tubulin. (F) PAVE complex was incubated with control or subtilisin-treated Taxol-stabilized bovine Cy5-microtubules as in (B) and imaged using epifluorescence. There is no difference in PAVE complex binding to subtilisin-treated microtubules cleaved of their C-terminal tails in comparison to control, indicating that the PAVE complex binds directly to the microtubule lattice.

<https://doi.org/10.1371/journal.ppat.1009588.g006>

ultracentrifugation to test its solubility. The majority of the complex remained in solution, suggesting that the PAVE complex is highly soluble (Fig 6A, right). These expression results, combined with their relationship in vivo, suggest that PAVE1 and PAVE2 form a hetero-oligomer that is responsible for the construction and maintenance of the tapered cell posterior.

To determine if the PAVE complex can bind directly to microtubules, we incubated the purified complex in solution with microtubules polymerized from bovine brain tubulin labeled with Cy5 dye (Fig 6B). The PAVE complex-microtubule mixture was added to a flow cell and allowed to attach to the surface, after which unbound protein was washed away and the flow cell was imaged using epifluorescence microscopy. The PAVE complex bound to microtubules at concentrations as low as 5 nM (Fig 6B). However, the PAVE complex did not crosslink microtubules into higher order structures such as bundles, regardless of the concentration of PAVE complex used or the length of the incubation. Although PAVE1 and thus PAVE2 as a direct binding partner may be components of the inter-microtubule crosslinks present at the *T. brucei* posterior subpellicular array in vivo, they appear to lack the capacity to organize microtubules into higher-order structures in vitro. These results show that PAVE1 and PAVE2 are true MAPs that directly interact with microtubules. Both proteins are smaller than most MAPs and lack repeats that frequently function as microtubule-binding sites, which suggests that they may have developed unique strategies for interacting with the subpellicular array [59,60].

Although the PAVE complex cannot bundle microtubules, we observed that it bound to microtubules in patches even at high nanomolar concentrations, rather than being distributed in a uniform manner along the length of the microtubule (Fig 6B). To determine how these patches form, we employed total internal reflection fluorescence (TIRF) microscopy to image the PAVE complex binding to microtubules. Cy5-labelled microtubules were attached to a flow cell, after which 5 nM PAVE complex was added into the chamber and immediately imaged using TIRF microscopy (S1 Movie). We saw that the PAVE complex bound to microtubules in discrete patches; these patches did not grow over time, although they did increase in intensity (Fig 6C, middle and right). Moreover, the PAVE complex patches were highly persistent. When patches were pre-seeded on microtubules in solution, added to a flow cell, and unbound complex was washed away, the pre-seeded patches remained for greater than 20 min and their distribution did not change (Fig 6D and S2 Movie). These results demonstrate that the PAVE complex binds to microtubules in static patches, which suggests that the complex

may recognize specific regions of microtubules. This static interaction may be modulated by other components of the subpellicular array that are not present in this assay, which could contribute to the migration of the PAVE complex towards the array anterior over the course of hours in intact cells (Fig 3).

Microtubules have many post-translational modifications (PTMs), which can differentially recruit MAPs or affect MAP behavior [27]. Most microtubule PTMs occur on their disordered C-terminal tails, which are also highly charged. We cleaved the C-terminal tails from bovine Cy5-labelled microtubules using subtilisin protease [61] to establish if the PAVE complex recognized tail-associated PTMs, which could explain its patchy localization pattern. We confirmed the removal of tubulin C-terminal tails by subtilisin using western blotting analysis (Fig 6E). We found that glutamylation, which is a modification that occurs exclusively on the C-terminal tail of  $\alpha$ - and  $\beta$ -tubulin, was significantly reduced by subtilisin treatment. Blotting with anti-tubulin antibody also showed that the protease-treated tubulin had undergone a molecular weight shift, indicating that the C-terminal tail had been removed. We incubated the PAVE complex with control and subtilisin-treated microtubules and found no difference in the intensity or pattern of binding, regardless of the concentration of PAVE complex used (Fig 6F). These results suggest that the PAVE complex binds directly to the microtubule lattice and may recognize a specific lattice structure rather than a post-translational modification in the tubulin tails. This result also indicates that the interaction of the PAVE complex with microtubules is not due to non-specific charge interactions with the highly acidic C-terminal tails of tubulin.

### TbAIR9 controls the distribution of PAVE1 in the subpellicular array

TbAIR9, which localizes to the entire subpellicular array, was also identified as a potential PAVE1 interactor in our immunoprecipitation analysis (Fig 4B). TbAIR9 shares sequence similarity with the microtubule associated protein AIR9 found in *Arabidopsis thaliana*, which has a role in positioning the phragmoplast during plant cytokinesis (Fig 4D) [62]. We tested whether depleting TbAIR9 had an effect on PAVE1. We conducted RNAi against TbAIR9 in a cell line where TbAIR9 was tagged with HA and PAVE1 was tagged with Ty1. Cells lacking TbAIR9 developed aberrant cell morphologies, including shortened posteriors, elongated cell bodies, and epimastigote-like DNA distribution, as previously reported (Figs 7A and S3A) [35]. These cells also ceased to divide, indicating that TbAIR9 is an essential protein (S3B Fig). During TbAIR9 RNAi, TbAIR9 signal was first lost at the posterior domain of the cell as previously reported (S3C Fig). In uninduced control cells, Ty1-PAVE1 strongly localized to the posterior and ventral edge of the cell, while in the absence of TbAIR9, PAVE1 lost its preference for the posterior subdomain and spread throughout the entirety of the array (Fig 7B). A line scan measuring PAVE1 intensity placed along the ventral edge of TbAIR9 RNAi cells showed that PAVE1 labeling was less intense at the cell posterior and more intense at the cell midzone and anterior in comparison to control cells (Fig 7C). PAVE1 protein levels were not altered, indicating that TbAIR9 depletion only affected the ability of PAVE1 to localize to the posterior subdomain (Fig 7D). Depleting PAVE1 from cells did not affect TbAIR9 stability or localization, except for its absence at the posterior subpellicular array in cells where the posterior was truncated (S3D and S3E Fig).

The mis-localization of PAVE1 could be due to the disruption of inter-microtubule crosslinks caused by TbAIR9 depletion. To determine if crosslinks are still formed in cells lacking TbAIR9, we created subpellicular array sheets of uninduced control and TbAIR9 RNAi cytoskeletons immunogold-labeled for Ty1-PAVE1 (Fig 7E). In control cells, crosslinks were present throughout the array, with PAVE1 localized along the ventral side of the microtubules and associated with intact crosslinks present at the cell posterior (Fig 7E, left). Crosslinks were still

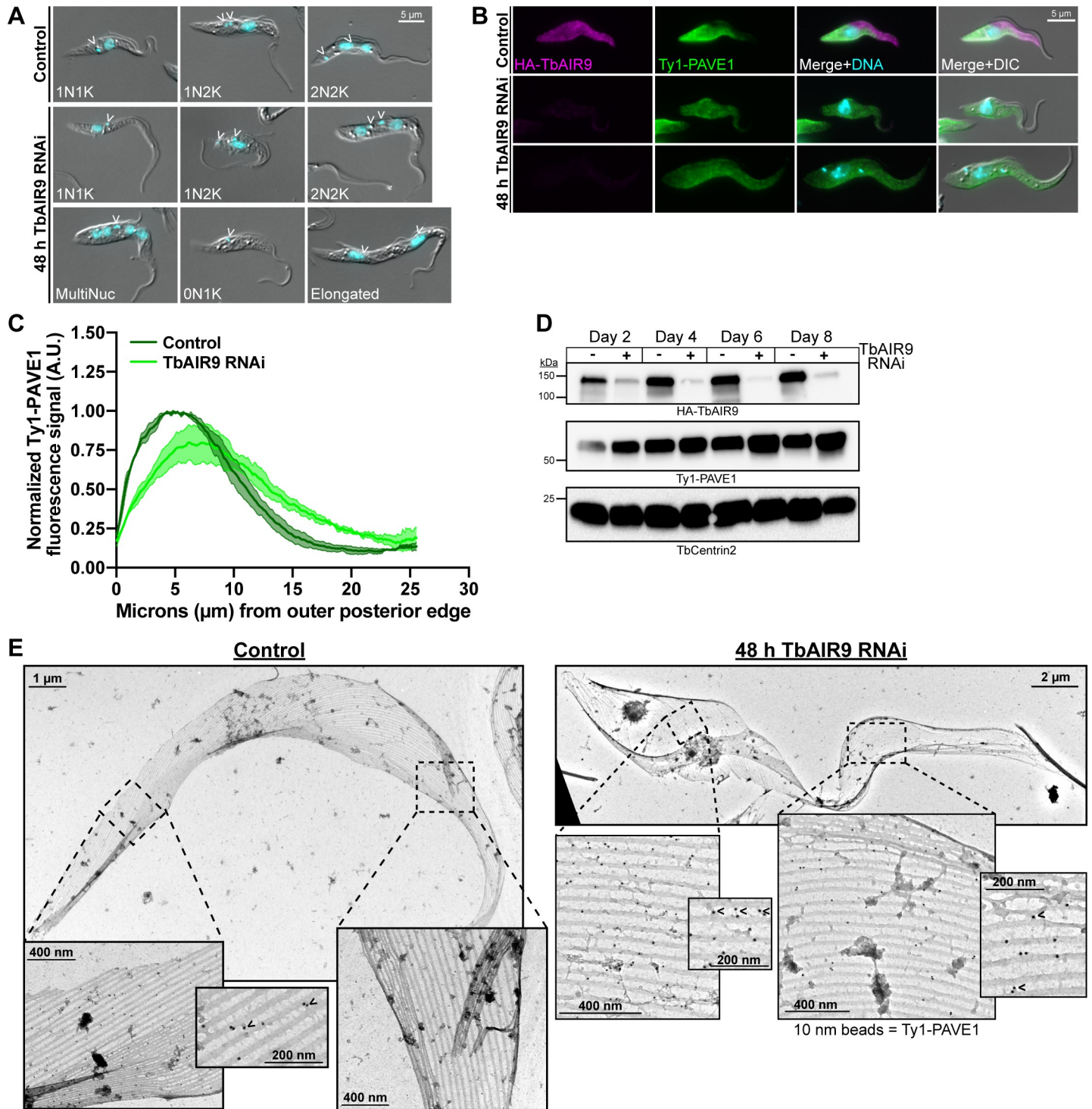


**Fig 7. TbAIR9 maintains PAVE1 at the cell posterior.** (A) Control and TbAIR9 RNAi cells were fixed in paraformaldehyde after 2 d of TbAIR9 depletion. Images are representative morphologies in control and TbAIR9 RNAi conditions. The epimastigote-like morphotype and elongated cell bodies were common in cells depleted of TbAIR9, as previously reported [35]. Open arrowheads indicate the kinetoplast. (B) Control and TbAIR9 RNAi cells were fixed in paraformaldehyde and stained after 2 d of TbAIR9 depletion. Ty1-PAVE1 signal is no longer maintained at the posterior and ventral edge. (C) The fluorescence signal intensity of Ty1-PAVE1 was measured along the ventral side of control and TbAIR9 RNAi cells after 2 d of TbAIR9 depletion. The signal intensities were normalized to the maximum control intensity, averaged, and plotted with the S.D. 50 1N1K cells in both control and TbAIR9 RNAi conditions from N = 3 independent biological replicates were measured. Ty1-PAVE1 signal is more evenly distributed throughout the array in TbAIR9 depleted cells than in control cells. (D) TbAIR9 RNAi was induced and lysates were collected every 48 h from control and TbAIR9 depleted cells. Lysates were separated by SDS-PAGE and transferred to nitrocellulose for western blotting. Ty1-PAVE1

signal remains stable during TbAIR9 depletion. (E) Subpellicular array sheets of control and TbAIR9 RNAi cells after 2 d of TbAIR9 depletion immunogold labeled against Ty1-PAVE1 with 10 nm beads. Ty1-PAVE1 localizes to the subpellicular microtubules at both the posterior and anterior ends of the array in the absence of TbAIR9. Open arrowheads indicate Ty1-PAVE1 beads on an inter-microtubule crosslink.

<https://doi.org/10.1371/journal.ppat.1009588.g007>

present throughout the array in TbAIR9 RNAi cells (Fig 7E, right), but PAVE1 was no longer confined to the posterior portion of the array. It was difficult to reliably produce sheets of whole TbAIR9 RNAi cells because the subpellicular array tended to fragment in these preparations. The fragility of TbAIR9 RNAi subpellicular arrays suggests that TbAIR9 has a role in promoting the integrity of the subpellicular array microtubules.

### TbAIR9 is a global regulator of subpellicular array-associated protein localization

The redistribution of PAVE1 throughout the array during TbAIR9 depletion led us to consider that TbAIR9 may regulate the localization of other cytoskeletal proteins in the subpellicular array. To test this, we identified two proteins that localized to different domains of the array using the whole-genome localization database TrypTag [63].

Tb927.9.10790 is a 33 kDa protein annotated by TrypTag as localizing to the middle of the subpellicular array. This protein is found only within the genomes of *T. brucei* and *T. cruzi* with no homologs present in other domains of life (Fig 8A). Tb927.11.1840 is a 45 kDa protein that localizes to the anterior array in TrypTag and appears to be unique to kinetoplastids (Fig 8B) [64]. Neither protein contained significant homology to known domains or motifs that we could identify. Tb927.9.10790 is predicted to be highly unstructured while Tb927.11.1840 contains predicted coiled coils [58,65]. We endogenously tagged both proteins at their C-termini and performed immunofluorescence on extracted cytoskeletons. Both 10790-Ty1 and 1840-Ty1 were stably associated with the cytoskeleton and localized to the midzone and anterior domains of the array, respectively (Fig 8A and 8B).

We next determined if TbAIR9 is necessary to maintain the distribution of 10790 and 1840 within their respective subdomains of the subpellicular array, as it does for PAVE1 at the array posterior (Fig 7). We induced TbAIR9 RNAi and localized 10790 and 1840 using immunofluorescence microscopy. We found that upon TbAIR9 depletion, 10790 is weakly distributed throughout the array (Fig 8C and 8E), while 1840 localized to both the posterior and anterior array, with weaker signal at the array midzone (Fig 8D and 8F). TbAIR9 RNAi decreased the protein levels of 10790 (S4A Fig), while 1840 protein levels increased (S4B Fig). These results suggest that TbAIR9 functions to organize and maintain array-associated proteins within discrete subdomains that exist within the *T. brucei* subpellicular array.

### Discussion

In this work, we have shown that the *T. brucei* subpellicular array is organized into subdomains defined by a unique distribution of microtubule associated proteins that may differentially regulate array microtubules and alter their local properties, such as their flexibility and curvature. Subpellicular arrays are also present in alveolates such as *Toxoplasma gondii* and *Plasmodium spp.*, where they play important roles in maintaining cell shape to facilitate infectivity. These arrays have fewer, more broadly spaced microtubules with stability-promoting MAPs that also localize to different regions of microtubules within the array [66–68]. Our work demonstrates that the concept of subdomains within microtubule arrays is conserved among highly divergent parasites and suggests a novel mechanism of microtubule array and cell shape regulation that may have broader implications in eukaryotic cell biology.

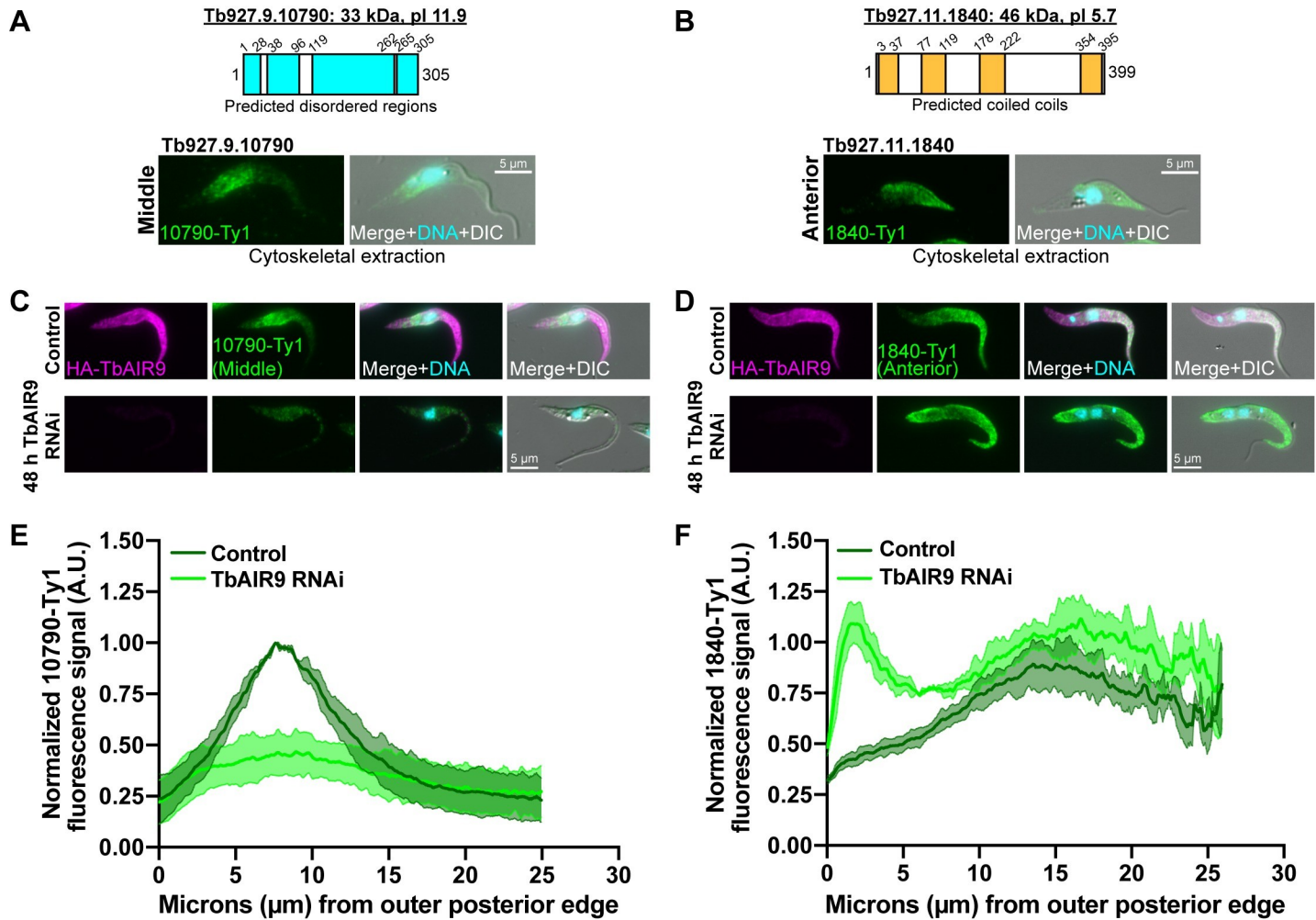


**Fig 8. TbAIR9 maintains the localization array-associated proteins at specific subdomains.** (A, B) Identification of array-associated proteins from TrypTag that localize to the middle subdomain (A, Tb927.9.10790) and the anterior subdomain (B, Tb927.11.1840). The schematics illustrate the predicted molecular weight (kDa) and pI for each protein. Tb927.9.10790 does not share homology with any known proteins, but it is predicted to be highly unstructured. Tb927.11.1840 also does not share homology with any known proteins, but it contains predicted coiled coils. Tb927.9.10790 and Tb927.11.1840 were tagged at their C-termini with Ty1 and a cytoskeletal extraction followed by immunofluorescence with anti-Ty1 antibody was performed. Tb927.9.10790 and Tb927.11.1840 remained bound to the middle and anterior subdomains of the following cytoskeletal extractions. (C,D) Cell lines containing 10790-Ty1 (C) and 1840-Ty1 (D) endogenous tags were fixed in paraformaldehyde and stained after 2 d of TbAIR9 depletion. 10790-Ty1 signal is depleted and spread throughout the cell body in the absence of TbAIR9, while 1840-Ty1 signal is detected at the posterior and anterior ends in TbAIR9 depleted cells. (E,F) Quantification of 10790-Ty1 (E) and 1840-Ty1 (F) fluorescent signal intensity along the ventral side of the cell body in TbAIR9 RNAi cells after 2 d of TbAIR9 depletion. The signal intensities were normalized to the maximum control values and plotted with the S.D. 50 IN1K cells in both control and TbAIR9 RNAi conditions from N = 3 independent biological replicates were measured.

<https://doi.org/10.1371/journal.ppat.1009588.g008>

In our analysis of potential array-associated proteins in the TrypTag database, the array posterior (represented here by PAVE1/2), middle (Tb927.9.10790), and anterior (Tb927.11.1840) were the most common localization patterns observed, suggesting that these regions are the primary subdomains of the array (Fig 9A) [63]. Many proteins also localize to the entirety of the array, such as TbAIR9. These primary subdomains each occur at unique places with respect to the flagellum and its attachment in *T. brucei*. The posterior subdomain comprises an area of the array that is not involved in flagellar attachment, as the flagellum exits onto the cell surface ~4–5  $\mu\text{m}$  from the posterior edge of the array. The middle subdomain covers the widest point of the cell body, directly after the flagellum exits the flagellar pocket and is attached to the cell surface. This includes the area where the flagellar pocket, kinetoplast,

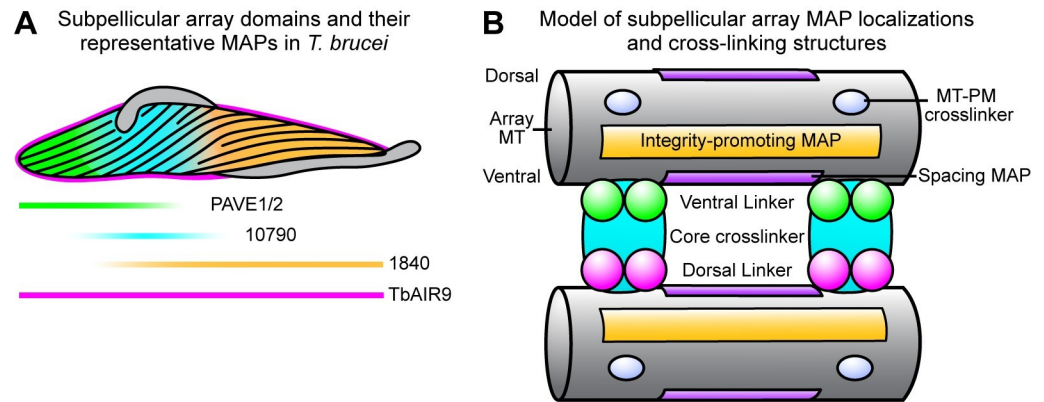


**Fig 9. Model of subpellicular array subdomains and potential MAP localizations in *T. brucei*.** (A) Three primary subdomains of subpellicular array regulation were identified in this work, represented by PAVE1/2, Tb927.9.10790, and Tb927.11.1840. TbAIR9, which localizes to the entire subpellicular array, is required to maintain the integrity of the subdomains. (B) A model for the potential MAP classifications and localizations in *T. brucei* as suggested by this work. MAP; microtubule associated protein. MT; microtubule. PM; plasma membrane.

<https://doi.org/10.1371/journal.ppat.1009588.g009>

and nucleus are located. The flagellum is attached throughout the entirety of the anterior subdomain, where the array rapidly tapers to a narrow point. The flagellar beat in *T. brucei* can initiate from either its base or tip and creates asymmetric waveforms along the cell body [5,69,70]. It is likely that each of these three subdomain regions experience different amounts of force during flagellar beating. The unique combination of array-associated proteins at each subdomain may be present to regulate microtubule flexibility and stability in response to these differential forces. The subdomain proteins may also be present to create the curvature and helicity of array microtubules and retain cell shape throughout the cell cycle, as is the case with PAVE1 and PAVE2. It is currently not known if there are ultrastructural variations in array architecture within these subdomains that would reflect the difference in protein composition. This is an important area for future ultrastructural investigation.

The specific function of nearly all of the array-associated proteins identified thus far is also unclear. Our work suggests that array-associated proteins serve a variety of roles in building the subpellicular array, from protecting microtubule integrity to generating the inter-microtubule crosslinks (Fig 9B). Subdomain-specific MAPs, like PAVE1 and PAVE2, may associate with core crosslinking proteins that span the inter-microtubule distance [33,34] to locally tune their properties. Other array-associated proteins may bind directly to microtubules to limit the placement of crosslinking fibrils, which would establish their regimented spacing [17,18]. This would require these MAPs to assemble in an organized manner that could measure length, perhaps like septin proteins [71]. Other MAPs may decorate microtubules to promote microtubule integrity, which could be the role of TbAIR9. Another category of array-associated proteins must form the smaller, similarly spaced fibrils that mediate attachment between the subpellicular array and plasma membrane, which is the proposed function of the protein WCB [36].

Our quantitative iEM shows that PAVE1 preferentially localizes to the ventral side of the subpellicular microtubules and may be a component of the inter-microtubule crosslinks at the cell posterior (Fig 2B–2D). While our ‘unroofing’ approach disrupts many of the inter-microtubule crosslinking fibrils, the spacing and length of the structures we observe coincide with the placement of the inter-microtubule crosslinks found by others in subpellicular array sheets [16,72]. Currently, there are no methods available for immuno-labeling intact inter-microtubule crosslinks, which are best visualized using electron tomography or quick-freeze deep-etch

EM [7,18,73]. The preferential localization of PAVE1 to the ventral side of microtubules suggests that inter-microtubule crosslinking fibrils are composed of asymmetrically distributed proteins and that PAVE1 contacts the microtubule on the ventral side of the crosslink (Fig 9B). The potential asymmetric composition of array crosslinks has also been suggested by WCB, which preferentially localizes to one side of the plasma-membrane facing surface of array microtubules [36,72].

PAVE1 is initially loaded onto the subpellicular microtubules at the extreme posterior end of the cell (Fig 3A). The growing plus-ends of subpellicular array microtubules are concentrated at this location throughout the cell cycle [16,40]. The PAVE complex is unlikely to be a microtubule plus-end binding protein, as its localization is not exclusive to the extreme posterior end where plus-end binders such as EB1 and XMAP215 are present [14,15,40] (Fig 2A). Recently, it has been suggested that several MAPs, including EB1 and the neuronal MAP doublecortin, preferentially recognize more open and irregular conformations of the microtubule lattice that are often present at microtubule plus-ends and sites of curvature or damage [28,29,74]. It is possible that PAVE1 may recognize irregularities in the microtubule lattice, which are concentrated at the polymerizing end of the microtubule where the lattice is incomplete. This would allow PAVE1 to interact with tubulin surfaces that are not usually accessible in assembled microtubule polymers [75]. It is also possible that polymerizing microtubule ends are the only places with free microtubule binding sites in the subpellicular array, as sites located more anterior in the array may already be occupied with different MAPs.

Our HaloTag capping assay shows that PAVE1 localization is not static within the array (Fig 3A–3C). PAVE1 migration towards the cell anterior suggests that the inter-microtubule crosslinking fibrils move within the array. This movement could be accomplished by several potential mechanisms. One possibility is that PAVE1 could be moved towards the cell anterior due to the intercalation of new microtubules into the existing array. Another possibility is that the inter-microtubule crosslinks may remain stably associated at their assembly sites along the microtubule lattice. As the microtubules turn over due to the addition of new tubulin at the cell posterior, the crosslinks migrate with the microtubules toward the anterior end of the cell. It is also possible that inter-microtubule crosslinks are not anchored to specific tubulin subunits in the lattice and can therefore diffuse along microtubules. In this case, the selective recruitment of new PAVE1 to the extreme posterior end drives the movement of extant crosslinks towards the cell anterior. Our in vitro data is more consistent with the PAVE complex forming persistent interactions with specific tubulin subunits. However, our use of Taxol-stabilized microtubules and the differences in the timescales monitored in our in vitro recombinant protein experiments (Fig 6) versus our in vivo capping experiments (Fig 3) cannot exclude slow diffusion of the PAVE complex along the array. The rapid rate of posterior end retraction upon PAVE1 depletion (Fig 3D) argues that the microtubules and inter-microtubule crosslinks are constantly being assembled and are essential for retaining the extended shape of the cell posterior. Since the subpellicular microtubules do not appear to undergo catastrophes that shorten them, this observation requires that cells that are not undergoing cell division have some process that removes tubulin subunits from the array at a similar rate to that which tubulin is added to the posterior end. Recently, it has been theorized that the microtubules of the array may ‘slide’ to the anterior end of the cell to accommodate remodeling events after cell division, which could be suggestive of a microtubule treadmilling process in the array [41].

TbAIR9, which is present throughout the entire array, appears to associate with the PAVE complex (Fig 4B and 4C) [35]. The phenotype of TbAIR9 depletion in *T. brucei* is complex and suggests a role of TbAIR9 in maintaining the structure of the subpellicular array. TbAIR9 RNAi results anucleate and multinucleated cells with elongated and epimastigote-like

morphologies (Figs 7A and S3A) [35]. TbAIR9 RNAi did not cause the inter-microtubule crosslinks to disappear (Fig 7E), but the complex cell morphologies produced by its depletion indicates it has a general role in array organization.

TbAIR9 appears to stabilize and protect the subpellicular array microtubules and regulate the positioning of array-associated proteins across subdomains. It was difficult to obtain array sheets from cells depleted of TbAIR9, indicating that the subpellicular array was more fragile in its absence (Fig 7E). The loss of the subdomain-specific localizations of PAVE1, Tb927.9.10790, and Tb927.11.1840 upon TbAIR9 RNAi (Figs 7 and 8) suggests that the structure of array microtubules is altered, perhaps creating a more open microtubule lattice that increases available binding sites for subdomain-specific MAPs across the array. The complex pleiomorphic phenotypes observed after TbAIR9 depletion could be due to the loss of array subdomains, which limits the parasite's ability to locally regulate microtubule properties and leads to a strong effect on processes such as cell division.

The subpellicular array microtubules must be sorted and partitioned in order to separate daughter cells during trypanosome cytokinesis. Very little is known about how this complex process is accomplished, although it appears to depend on molecular motors and the careful maintenance of cell shape. The microtubule severing enzymes spastin and katanin are required for array partitioning and the completion of abscission [76]. The recently identified orphan kinesin KLIF is also necessary for array separation, as KLIF RNAi blocks cell separation after cytokinesis initiation, resulting in partially ingressed furrows [43,77]. Small alterations in array shape have profound impacts on the fidelity of cytokinesis in *T. brucei*. Two kinetoplastid-specific kinesins, TbKIN-C and TbKIN-D, maintain the shape of the array posterior and its organization as a single layer of microtubules [78,79]. Depletion of these kinesins results in misplaced cleavage furrows and an eventual block in cytokinesis. As evidenced by our work, the shortening of the array posterior is the first consequence of PAVE1/2 depletion (Figs 3C and 5D). This appears to result in acute cytokinetic defects, including the misplacement of the cleavage furrow and the complete inhibition of cytokinesis (Figs 5 and S2A). The depletion of TbAIR9 also creates shape changes in the array (Fig 7A), which appears to primarily result in the misplacement of the cleavage furrow, producing significant amounts of anucleate cells (S3B Fig). These phenotypes suggest that the elaborate array architecture and the tight organization of array microtubules is necessary and required for proper division and morphogenesis in these parasites.

Our work has highlighted the potential functions of a set of proteins that are components of distinct subdomains within the subpellicular array. While the PAVE complex appears to function to maintain the length and shape of the array microtubules at the cell posterior, the functions of Tb927.9.10790 and Tb927.11.1840 are yet to be determined. Future work is also needed to discover how TbAIR9 regulates microtubules to organize these proteins into defined domains across the array. The TrypTag database contains many previously unidentified proteins that appear to localize to the subpellicular array within these subdomains. Uncovering the function of a broad range of array-associated proteins is essential for understanding subpellicular array biogenesis and how trypanosomatids tune parasite shape and motility to survive within their hosts.

## Materials and methods

### Antibodies

Antibodies are from the following sources and were used at the following dilutions: anti-Ty1 (1:1000 for immunofluorescence and western blotting; 1:50 for immunogold labeling) from Sebastian Lourido (Massachusetts Institute of Technology—Boston, MA), TAT1 (1:100) from

Jack Sunter (Oxford Brookes University—Oxford, United Kingdom). YL1/2 (1:4,000) was purchased from ThermoFisher Scientific (Waltham, MA, cat# MA1-80017) and anti- $\alpha$  tubulin (1:10,000) was also purchased from ThermoFisher Scientific (clone B-5-1-2). Anti-HA antibody (1:500) was purchased from Sigma-Aldrich (St. Louis, MA, clone 3F10). GT335 (1:25,000) was purchased from Adipogen (San Diego, CA, cat# AG-20B-0020-C100). Anti-TbCentrin2 (1:150) antibody was previously described [80].

## Cell culture

Wild-type procyclic *T. brucei brucei* 427 strain cells and the doxycycline-inducible 29–13 *T. brucei* cell line [81] were used to perform experiments. 427 cells were passaged in Beck's Medium (Hyclone—GE Healthcare, Logan, Utah) supplemented with 10% fetal calf serum (Gemini Bioproducts—West Sacramento, CA), while 29–13 cells were passaged in Beck's Medium supplemented with 15% doxycycline-free fetal calf serum (R&D Systems—Minneapolis, MN), 50  $\mu\text{g mL}^{-1}$  hygromycin (ThermoFisher Scientific), and 15  $\mu\text{g mL}^{-1}$  G418 (Sigma-Aldrich). 427 and 29–13 media also included 10  $\mu\text{g mL}^{-1}$  gentamycin (ThermoFisher Scientific) and 500  $\mu\text{g mL}^{-1}$  penicillin-streptomycin-glutamine (ThermoFisher Scientific). All cells were maintained at 27°C. Cells were counted using a particle counter (Z2 Coulter Counter, Beckman Coulter—Brea, CA).

## Cloning and cell line construction

All constructs were created by PCR amplification of inserts from *T. brucei* genomic DNA using Q5 polymerase (NEB—Ipswich, MA) followed by either restriction-ligation or Gibson Assembly into a sequencing vector (PCR4Blunt) or a modified pLEW100 for long-hairpin RNAi (lhRNAi) generation as previously described [82]. Each DNA construct was validated by sequencing and transfected into cells using an electroporator (GenePulser xCell, Bio-Rad—Hercules, CA). Clonal cell lines were created by selection and limiting dilution. Cell lines were validated with western blotting and loci PCRs. All sequences were obtained from TriTrypDB [64].

**RNAi constructs.** Sequences for RNAi were selected from the coding sequence of the target protein using the RNAi online tool (<https://dag.compbio.dundee.ac.uk/RNAi/>) [83]. 400–600 base pairs were used to create lhRNAi constructs as follows: PAVE1 (Tb927.8.2030)—bp 97–543; PAVE2 (Tb927.9.11540)—bp 514–1112; TbAIR9 (Tb927.11.17000)—bp 1868–2303. Constructs were linearized for transfection with NotI (NEB) and transfected into the 29–13 cell line, after which clonal populations were obtained by selection with 40  $\mu\text{g mL}^{-1}$  Zeocin (Life Technologies—Carlsbad, CA).

**Endogenous tagging constructs.** Endogenous tagging constructs were created using Gibson Assembly into the PCR4Blunt sequencing vector. N-terminal tagging constructs (PAVE1, PAVE2, TbAIR9) were targeted to their respective endogenous loci using last 500 bp of 5' UTR and first 500 bp of the coding sequence. C-terminal tagging constructs (Tb927.9.10790, Tb927.11.1840) were targeted to their loci using the last 500 bp of the coding sequence followed by the first 500 bp of the 3' UTR. Endogenous tagging constructs were excised using PacI and NsiI (NEB) and transfected into either the 427 or 29–13 cell lines, and clonal populations were selected using 10  $\mu\text{g mL}^{-1}$  blasticidin or 1  $\mu\text{g mL}^{-1}$  puromycin.

## Image acquisition for fluorescence microscopy

**Epifluorescence acquisition.** Images were acquired using a Zeiss Axio Observer.Z1 microscope (Carl Zeiss Microscopy—Oberkochen, Germany) using an 100X/1.4 NA Plan-Apochromat oil lens with an ORCA-Flash 4.0 V2 CMOS camera (Hamamatsu—Shizuoka, Japan). Z-stacks were acquired for each image.

**Total internal reflection fluorescence acquisition.** Images were acquired at RT with the same Zeiss Axio Observer.Z1 microscope described above, equipped with a spinning illumination ring VectorTIRF system which includes a 405/488/561/640 quad band dichroic filter (Intelligent Imaging Innovations, Inc.—Denver, CO) and an Alpha Plan-Apochromat 100X/1.46 NA oil TIRF objective. Samples were excited using 488 nm 150mW and 647 nm 120mW lasers at 20% power. Images were acquired every 10 sec for 20 min using a Prime 95B Back Illuminated Scientific CMOS camera (Teledyne Photometrics—Tucson, AZ) and a Definite Focus.2 system (Carl Zeiss Microscopy) for automatic focus correction.

SlideBook 6 digital microscopy software (Intelligent Imaging Innovations, Inc.) was used to manipulate the microscope and acquire images. Images were analyzed with ImageJ (National Institutes of Health—Bethesda, MD) and exported to Adobe Photoshop and Illustrator (CC 2020) for publication.

### Immunofluorescence microscopy

Cells were harvested from culture by centrifugation at 2400  $\times$  g for 5 min and washed with PBS. Cells were centrifuged onto coverslips and fixed as per the conditions below. All fixation conditions for each experiment are specified in the text and figure legends. After fixation, cells were washed 3X with PBS and blocked using 5% goat serum (ThermoFisher) in PBS for either 20 min RT or overnight at 4°C. Coverslips were then incubated with primary antibody diluted into blocking buffer for 1 hr RT, after which they were washed 3X with PBS and incubated with secondary antibody conjugated to Alexa Fluor -647, -568, and -488 (Life Technologies) diluted 1:1000 in blocking buffer for 1 hr RT. Coverslips were washed a final 3X with PBS and mounted for epifluorescence imaging using Fluoromount-G with DAPI (Southern Biotech—Birmingham AL).

**Methanol fixation.** After cells were centrifuged onto coverslips, excess PBS was wicked away with tissue paper and the coverslips were quickly plunged into -20°C methanol for 20 min.

**Paraformaldehyde fixation.** Coverslips were inverted onto a drop of 4% paraformaldehyde in PBS for 20 min RT in a humidified chamber. Cells were permeabilized by moving the coverslip to a drop of 0.25% NP-40 (IPEGAL CA-630, Sigma Aldrich) in PBS for 5 min RT.

**Cytoskeletal extraction.** Coverslips were inverted onto a drop of cytoskeletal extraction buffer (0.1 M PIPES pH 6.9, 2 mM EGTA, 1 mM MgSO<sub>4</sub>, 0.1 mM EDTA, 0.25% NP-40) for 2 min RT. Coverslips were then quickly washed 6X with PBS and fixed for 20 min RT with 4% paraformaldehyde in PBS.

### Transmission electron microscopy

**Whole-mount extracted cytoskeletons preparation.** Cells were harvested by centrifugation at 800  $\times$  g and washed 3X with PBS. Cells were briefly spun onto glow-discharged formvar- and carbon-coated grids (Electron Microscopy Sciences—Hatchfield, PA) at 800  $\times$  g. Grids were floated on two subsequent drops of cytoskeletal extraction buffer [0.1 M PIPES pH 6.9, 2 mM EGTA, 1 mM MgSO<sub>4</sub>, 0.1 mM EDTA, 1% NP-40] for 3 min RT each drop, and then briefly washed in a drop of extraction buffer without detergent. Grids were fixed in a drop of 2.5% glutaraldehyde in PBS for 5 min RT, after which they were washed with distilled water and negatively stained with 1% aurothioglucose for 6 sec (Sigma Aldrich).

**Immunogold labeling.** Whole-mount extracted cytoskeletons were prepared as above, but prior to fixation, cells were blocked by quickly moving the grids through 5 drops of blocking buffer (2% bovine serum albumin in PBS). Grids were incubated for 1 hr RT in primary antibody diluted in blocking buffer, after which they were washed 5X with blocking buffer.

Grids were then incubated with 10 nm or 20 nm gold-conjugated secondary antibodies (BBI Solutions—Newport, United Kingdom) diluted 1:25 in blocking buffer for 1 h RT. Grids were fixed and stained as above.

**Subpellicular sheeting.** Cells were prepared for sheeting as described in [16]. After cells were centrifuged onto grids and extracted as above, the grids were gently fixed in a primary fixative of 3.2% paraformaldehyde in cellular extraction buffer without detergent for 5 min RT. The paraformaldehyde was then quenched by incubating the grids in 20 mM glycine in PBS for 5 min RT. Grids were blocked and immunogold labeled as above. After labeling, grids were fixed with 2.5% glutaraldehyde in PBS for 5 min RT, washed 2X with distilled water, and positively stained in a drop of 2% aqueous uranyl acetate for 45 min RT. Grids were dehydrated in an ethanol series (30%-50%-70%-90%-3X 100%; 10 min RT each condition) and critical point dried. The top layer of the subpellicular array was removed to ‘unroof’ the cells by inverting the grid onto double-sided tape, applying gentle pressure, and then lifting the grid off the tape.

**Image acquisition for TEM.** Images were taken on a Phillips 410 transmission electron microscope at 100 kV equipped with a 1k x 1k Advantage HR CCD camera from Advanced Microscopy Techniques (AMT) using AMT imaging software. Images were analyzed in ImageJ and exported to Adobe Photoshop and Illustrator for processing.

**Quantification of immunogold label distribution on subpellicular sheets.** Micrographs of subpellicular sheets in which the flagellum was still attached were analyzed in ImageJ. The sheets were oriented along the dorsal-ventral axis using the flagellum as a fiducial marker. A 1  $\mu\text{m}^2$  area of the sheet was selected for analysis. Each microtubule within the 1  $\mu\text{m}^2$  area was traced using the segmented line tool. A semi-automated macro was written in ImageJ which converted the segmented line into a spline-fit line and straightened the microtubule according to the spline curve. A rectangle was placed on the bounding edges of the straightened microtubule and its centroid was calculated and plotted. The location of each gold bead on the microtubule was manually counted as dorsal (above the centroid line), centroid (touching the centroid line) or ventral (below the centroid line), as well whether the gold bead localized to an inter-microtubule crosslink. Three subpellicular array sheets were analyzed per N = 3 independent biological replicates for each experiment. The data were recorded in Microsoft Excel and statistical tests were performed and the data graphed using Prism 8 (Graphpad).

### HaloTag capping assay

HaloTag [50] substrate conjugated to JF646 (Promega—Madison, WI) was added to a culture of  $2 \times 10^6$  cell  $\text{mL}^{-1}$  log-phase HaloTag-PAVE1 cells at a final concentration of 2  $\mu\text{M}$  for 1 h at 27°C. Cells were collected by centrifugation at 2400  $\times g$  and washed 3X with Beck's Medium. Cells were resuspended at  $2 \times 10^6$  cell  $\text{mL}^{-1}$  in complete media and HaloTag substrate conjugated to TMR (Promega) was added at a final concentration of 5  $\mu\text{M}$ . Cells were harvested at T = 0 h, T = 1 h, T = 3 h, and T = 8 h of TMR substrate addition by centrifugation at 2400  $\times g$ . Cells were washed 3X with HBSS, centrifuged onto coverslips, and fixed for 20 min RT with 4% paraformaldehyde in PBS. Coverslips were washed 3X with PBS and mounted with Fluoromount-G containing DAPI.

**Image acquisition and fluorescence intensity analysis.** Images were captured using epifluorescence as above. Maximum projections of each Z-stack were created and background-corrected using rolling ball background subtraction (radius = 100 pixels). The ventral edge of 50 IN1K cells per time point was traced on the DIC image of the cells using the segmented line tool. The fluorescence intensity along each line for HaloTag substrates conjugated to JF646 and TMR were recorded and exported to Microsoft Excel. The average pixel intensity and S.D.

at each position along the line was calculated and normalized to 1 from  $N = 3$  independent biological replicates and graphed using Prism 8 software.

## RNAi

Log-phase cultures of 29–13 cells containing lhRNAi constructs were seeded at  $1 \times 10^6$  cell  $\text{mL}^{-1}$ . RNAi was induced in using  $1 \mu\text{g mL}^{-1}$  doxycycline (ThermoFisher Scientific) or 70% ethanol as a vehicle control. Cell growth was recorded every 24 h unless otherwise noted, and samples were collected for western blotting or immunofluorescence. RNAi cultures were re-seeded every 48 h in fresh media and doxycycline or ethanol was added as above. All RNAi generation plots represent three independent biological replicates and the error bars are the S.D.

## PAVE1 and PAVE2 RNAi image analysis

Control and RNAi cells were fixed in methanol or paraformaldehyde and stained as above. Maximum projections of each Z-stack were created for analysis. For the short time course of PAVE1 RNAi: cells were harvested and fixed in methanol after  $T = 0$  h, 4 h, and 6 h after RNAi induction, and stained for  $\alpha$ -tubulin as described above. Only 1N2K cells were selected for analysis, as these cell types have progressed over halfway through the cell cycle at the time of harvest [39], and defects in the array would be due solely to PAVE1 RNAi, and not defects in cytokinesis or G1 subpellicular array remodeling. 50 1N2K cells per each time point in  $N = 3$  independent biological replicates were measured. The distance from the posterior kinetoplast to the outer posterior edge of the subpellicular array, as well as the posterior nucleus edge to the posterior kinetoplast, were measured. For PAVE2 RNAi: Cells were harvested and fixed in paraformaldehyde, and stained for  $\alpha$ -tubulin as described above. For DNA state analysis, 300 cells for each time point in control and PAVE2 RNAi conditions were counted in  $N = 3$  independent biological replicates. For posterior end measurements, 100 1N1K cells in control and 1 PAVE2 RNAi conditions were measured as above in  $N = 3$  independent biological replicates. Data were recorded in Microsoft Excel and statistical tests were conducted and the data graphed using Prism 8.

**PAVE1, Tb927.9.10790, Tb927.11.1840 fluorescence intensity analysis during TbAIR9 RNAi.** Control and TbAIR9 RNAi cells were harvested after 2 d of RNAi induction and fixed in paraformaldehyde and stained with anti-Ty1 and anti-HA antibodies as above. The ventral side of 1N1K cells was traced along the DIC image of the cell using the segmented line tool, and fluorescence intensities were recorded and analyzed as above and normalized to the maximum control value. 50 1N1K cells each were measured in control and TbAIR9 RNAi conditions for  $N = 3$  independent biological replicates for each cell line.

## SDS-PAGE and western blotting

*T. brucei* cells were collected by centrifugation at  $2400 \times g$ , washed with PBS, lysed in SDS-PAGE lysis buffer and incubated for 10 min at  $99^\circ\text{C}$ .  $3 \times 10^6$  cell equivalents/lane were separated by SDS-PAGE and transferred to a nitrocellulose membrane. Blots were blocked with 5% (w/v) non-fat dry milk dissolved in TBS containing 0.1% Tween-20 for 1 hr RT and incubated overnight at  $4^\circ\text{C}$  with primary antibody diluted in blocking buffer. Blots were washed 3X with TBS containing 0.1% Tween-20 and incubated for 1 hr RT with secondary antibody conjugated to horseradish peroxidase diluted into blocking buffer (Jackson ImmunoResearch—West Grove, PA). Blots were washed a final 3X and imaged using Clarity Western ECL substrate (BioRad) and a BioRad Gel Doc XR+ system.

## Immunoprecipitation of mNeonGreen-PAVE1

Both endogenous alleles of PAVE1 were tagged at their N-termini with mNeonGreen [84] as described above.  $3\text{--}8.0 \times 10^8$  WT 427 control and mNeonGreen-PAVE1 cells were harvested and lysed in lysis buffer [10 mM  $\text{Na}_3\text{PO}_4$  pH 7.4, 150 mM NaCl, 0.5% glycerol, 7% sucrose, and 0.5% NP-40 with 1 mM DTT; 1mM PMSF and 1X HALT (ThermoFisher) were added as protease inhibitors]. Cytoskeletal proteins were solubilized by sonication, after which the lysate was clarified by centrifugation at  $17.1\text{K} \times g$  for 20 min at  $4^\circ\text{C}$ . Cleared supernatant material was diluted by half to decrease the concentration of detergent and incubated with magnetic beads conjugated to the camelid nanobody mNeonGreen-Trap (Chromotek—Munich, Germany) for 1 hr  $4^\circ\text{C}$ . The beads were washed 6X with lysis buffer without glycerol, sucrose, and detergent. Beads were immediately processed for mass spectrometry, or bound proteins were eluted by adding SDS-PAGE lysis buffer and incubating the beads at  $99^\circ\text{C}$  for 10 min. Eluted proteins were separated by SDS-PAGE and the gel was silver stained (ThermoFisher Scientific) for imaging.

## Mass spectrometry

**On-beads sample preparation of control and mNeonGreen-PAVE1 immunoprecipitates.** The supernatants from mNeonGreen-PAVE1 and corresponding 427 WT control immunoprecipitations were removed and replaced with  $100 \mu\text{L}$  0.1 M ammonium bicarbonate in water. Cys residues were reduced and alkylated using 5 mM dithiothreitol in 0.1 M ammonium bicarbonate for 1.5 hr, and 10 mM iodoacetamide in 0.1 M ammonium for 45 min in the dark, respectively. Both reactions proceeded at  $37^\circ\text{C}$  in a thermal mixer. A 16 hr,  $37^\circ\text{C}$  on-beads tryptic digestion was performed on a thermal mixer with constant agitation using a 1:20 (w/w) enzyme: protein ratio for Promega modified sequencing grade trypsin. Tryptic peptides were then removed and the digestion was quenched by the addition of concentrated formic acid to yield a final pH of 3. Proteolytic peptides were desalted using Pierce C18 Spin Columns (ThermoFisher Scientific) per manufacturer's instruction, dried to completion, resuspended in 0.1% formic acid in water (Solvent A) and quantified using a Thermo Scientific Nanodrop Spectrophotometer.

**Mass spectrometry-based proteomics analysis.** NeonGreen-PAVE1 and WT 427 control peptide sample concentrations were matched using Solvent A prior to injection onto a Waters  $75 \mu\text{m} \times 250 \text{mm}$  BEH C18 analytical column using a Thermo Scientific Ultimate 3000 RSLCnano ultra-high performance liquid chromatography system directly coupled to a Thermo Scientific Q Exactive HF Orbitrap mass spectrometer. A 1 hr, linear reversed-phase gradient (Solvent B: 0.1% formic acid in acetonitrile) at  $300 \text{nL}/\text{min}$  flow was used to separate peptides prior to mass analysis. Peptides were ionized directly into the Q Exactive HF via nanoflow electrospray ionization. High energy collision dissociation (HCD) MS/MS peptide interrogation was achieved using a top 15 data-dependent acquisition method in positive ESI mode. All raw data were searched against the Uniprot *T. brucei* reference proteome (identifier AUP000008524, database accessed 09/11/2018 and updated 04/27/2018) plus the full mNeonGreen-PAVE1 protein sequence using the MaxQuant software suite [85]. Search parameters included the following: 1% false discovery rate cutoff at the protein and peptide-spectrum match levels, trypsin cleavage specificity with 2 missed cleavages, 5 amino acids/peptide minimum, and the "LFQ" algorithm was used to provide label-free quantitation. All other MaxQuant parameters were kept at default values. Search output files were compiled into Scaffold Q+S (Proteome Software, Inc.) for data visualization and further analysis.

## Recombinant expression and purification of the PAVE complex

For recombinant expression in bacteria, the entire coding sequences of PAVE1 and PAVE2 were amplified from *T. brucei* genomic DNA. The solubility-enhancing maltose-binding

protein (MBP) was fused to an oligo-His<sub>10</sub> tag followed by a TEV protease site and appended to the N-terminus of mNeonGreen-PAVE1. The MBP-oligoHis-TEV-mNeonGreen-PAVE1 construct was inserted into a MalpET expression vector containing kanamycin resistance. The Strep-tag [86] peptide sequence was appended to the N-terminus of PAVE2 and inserted into a pOKD5 expression vector containing ampicillin resistance. Both vectors were co-transformed into BL21 (DE3) bacteria. 0.5 L of cells were grown to mid-log phase (OD<sub>600</sub> ~0.6) and overexpression of the proteins were induced by adding 0.4 mM IPTG at 16°C overnight. Cells were collected by centrifugation and lysed in lysis buffer [100 mM Tris pH 8.0, 300 mM NaCl, 0.5% NP-40, 0.5 mM DTT, with the addition of 1 mM PMSF and 1X HALT]. After sonication, the lysate was clarified by centrifugation at 17K *x g* and the supernatant was batch-incubated for 45 min at 4°C with 3 mL of Ni-NTA agarose resin that had been pre-treated with 0.5 M imidazole pH 7.4 followed by equilibration with lysis buffer (ThermoFisher Scientific). The protein-bound resin was passed over a column and washed with 20 column volumes of Wash10 buffer [100 mM Tris pH 8.0, 300 mM NaCl, 0.5 mM DTT, 10 mM imidazole] followed by 20 column volumes of Wash30 buffer [100 mM Tris pH 8.0, 300 mM NaCl, 0.5 mM DTT, 30 mM imidazole]. Bound proteins were eluted in 1 mL fractions using elution buffer [100 mM Tris pH 8.0, 300 mM NaCl, 0.5 mM DTT, 200 mM imidazole]. Peak fractions were pooled and dialyzed overnight at 4°C into Strep buffer [100 mM Tris pH 8.0, 150 mM NaCl, 1 mM EDTA]. Dialyzed fractions were treated with TEV protease (1:25 molar ratio) to remove the MBP-oligoHis<sub>10</sub>-TEV fusion from mNeonGreen-PAVE1 for 5 hr RT, after which the complex was passed over Strep-Tactin XT resin (IBA Lifesciences—Goettingen, Germany). Bound complex was eluted using Buffer BXT containing 50 mM biotin (IBA Lifesciences). Protein samples were diluted into SDS-PAGE lysis buffer and incubated at 99°C for 10 min for separation by SDS-PAGE and Coomassie staining. Purified PAVE complex was then dialyzed into storage buffer [100 mM Tris pH 8.0, 300 mM NaCl, 1 mM DTT, 50% glycerol] overnight at 4°C. This preparation typically yielded ~200 µg of total protein that was stable for several months at -20°C.

### In vitro microtubule interaction assays

Cycled bovine tubulin (PurSolutions—Nashville, TN) was thawed and centrifuged at 400,000K at 2°C for 6 min. Clarified tubulin was diluted to 100 µM in ice-cold BRB80 buffer [80 mM PIPES pH 6.9 with KOH, 1 mM EGTA, 1 mM MgCl<sub>2</sub>] and mixed with in a 1:5 ratio with 20 mg mL<sup>-1</sup> Cy5-labeled bovine tubulin (PurSolutions). Tubulin was polymerized for 20 min at 37°C then stabilized with 10 µM Taxol (Cytoskeleton Inc.—Denver, CO) as previously described [43,87]. Tubulin was stored at RT for up to 2 d for use in experiments. The PAVE complex was clarified to remove aggregates by ultracentrifugation at 400K *x g* at 2°C for 15 min before use in subsequent experiments.

**In-solution microtubule binding experiments.** 5–500 nM PAVE complex was mixed with 0.5 µL of microtubules diluted in 50 µL of blocking buffer [10 mM imidazole pH 7.4, 50 mM KCl, 1 mM EGTA, 4 mM MgCl<sub>2</sub> supplemented with 2 mg mL<sup>-1</sup> κ-casein, 0.1% Plurionic F-68 (ThermoFisher Scientific), 10 µM Taxol, and an oxygen-scavenging system (3 mg mL<sup>-1</sup> glucose, 0.1 mg mL<sup>-1</sup> glucose oxidase and 0.18 mg mL<sup>-1</sup> catalase)] and incubated for 20 min RT. Flow cells were constructed from glass coverslips and treated with rigor-like kinesin to attach microtubules to the glass surface as previously described [43,87]. The flow cells were then blocked with two 20 µL passages of blocking buffer. The PAVE complex-microtubule mixture was passed over flow cells, and any complex-microtubule mixture not captured by the rigor-like kinesin was washed away with two 20 µL passages of blocking buffer. Flow cells were imaged using epifluorescence as above. Figures are representative of three independent biological replicates using two separate PAVE complex preparations.

**Total internal reflection fluorescence microscopy experiments.** EGYlated flow cells were prepared to minimize background as previously described [87]. Briefly, glass coverslips were plasma cleaned for 5 min and sonicated in 1M KOH for 20 min. Coverslips were extensively washed with ddH<sub>2</sub>O followed by 95% ethanol and dried using a stream of N<sub>2</sub>. Slides were then incubated for 90 min RT in coating solution placed in glass beakers [97.65% toluene, 1.73% methoxy(polyethyleneoxy)propyltrimethoxysilane, 0.62% n-butylamine]. The glass beakers were placed in a plastic bag filled with N<sub>2</sub> to remove oxygen, which can interfere with the treatment of the glass slides. Slides were washed twice with 100% toluene, dried with N<sub>2</sub>, prepared as flow cells, and stored at -20°C for up to 6 months for use.

Rigor-like kinesin was passed over the PEGylated flow cell, followed by two passages of blocking buffer. For the PAVE complex binding experiment, 0.5 μL of microtubules diluted in 50 μL blocking buffer were passed through the flow cell and allowed to attach to the rigor-like kinesin on the PEGylated surface, after which unbound microtubules were washed away with two 20 μL passes of blocking buffer. 5 nM PAVE complex was added to the flow cell and immediately imaged using TIRF microscopy. For the PAVE complex patch stability experiment, 5 nM PAVE complex patches were pre-seeded in solution on microtubules prepared as above for 10 min RT and passed through the flow cell. Unbound material was removed with three 20 μL washes of blocking buffer, after which the flow cell was imaged using TIRF microscopy. Figures and movies are representative of three independent biological replicates using two separate PAVE complex preparations.

**Subtilisin-treated microtubule binding assay.** The C-terminal tails of Taxol-stabilized Cy5 microtubules were cleaved using Subtilisin A (Sigma Aldrich) as previously described [88]. A 1:15 molar ratio of microtubules to subtilisin A were diluted into BRB80 blocking buffer [80 mM PIPES pH 6.9 with KOH, 1 mM MgCl<sub>2</sub>, 1 mM EGTA, supplemented with 2 mg mL<sup>-1</sup> κ-casein, 0.1% Plurionic F-68, 10 μM Taxol, and an oxygen-scavenging system as above] and incubated for 45 min at 30°C. The cleaving reaction was stopped with the addition of 10 mM PMSF for 10 min at 30°C. Samples of the microtubules were diluted into SDS-PAGE lysis buffer and incubated at 99°C for 10 min for western blotting to confirm tail cleavage as above. Control or subtilisin-treated microtubules were incubated with 5 nM or 50 nM PAVE complex for 20 min RT and passed over prepared glass flow cells and imaged using epifluorescence as described above. Figures are representative of four independent biological replicates using one PAVE complex preparation.

## Supporting information

**S1 Fig. Quantification methodology used to classify immunogold label distribution in subpellicular array sheets.** (A) A whole-mount extracted cytoskeleton immunogold-labeled for Ty1-PAVE1 with 20 nm beads. (B) A semi-automated macro was written in ImageJ to facilitate the classification gold bead distribution as dorsal, centroid, or ventral, as well as cross-link associated, along individual microtubules of subpellicular array sheets. (TIF)

**S2 Fig. PAVE1 and PAVE2 require each other for stability in vivo.** (A) Generation plot of cell growth after induction of PAVE2 RNAi. The cell density was monitored every 24 h in control and PAVE2 RNAi conditions. The curve is the mean of N = 3 independent biological replicates. (B) Lysates were collected every 24 h from control and PAVE2 RNAi cells during 6 d of PAVE2 depletion. Lysates were western blotted with antibodies against HA and TbCentrin2 as a loading control. (C) Lysates from control and PAVE1 RNAi cells in which PAVE2 is endogenously tagged were collected for western blotting every 24 h during PAVE1 depletion. Duplicate lysates were western blotted, as PAVE1 and PAVE2 are the same molecular weight. (D)

Lysates from control and PAVE2 RNAi cells in which PAVE1 is endogenously tagged were collected for western blotting every 24 h during PAVE2 depletion. The lysates were blotted in duplicates as in (C).

(TIF)

**S3 Fig. TbAIR9 does not require PAVE1 for localization or stability in vivo.** (A) Quantification of DNA states of paraformaldehyde-fixed cells after 2 d of TbAIR9 RNAi. 0NXK; anucleate cells. MultiNuc; multinucleated cells. Epimastigote-like cells were cells in which the kinetoplast was located at the midline and anterior to the nucleus; 0NXK and MultiNuc were excluded from this analysis. 200 cells were counted from N = 3 independent biological replicates.

\*P<0.05, \*\*P<0.005, \*\*\*P<0.001. P-values are calculated from unpaired two-tailed Student's *t*-tests using the average from N = 3 independent biological replicates. (B) Generation plot of cell growth after induction of TbAIR9 RNAi. Cell concentration was monitored in control and TbAIR9 RNAi cells every 24 h. The curve is the mean of N = 3 independent biological replicates. (C) Control and TbAIR9 RNAi cells were fixed with paraformaldehyde and stained after 24 h of TbAIR9 depletion. TbAIR9 localization initially disappears from the cell posterior during TbAIR9 RNAi, as previously reported. (D) PAVE1 RNAi was induced in cells in which TbAIR9 is endogenously tagged with the HA epitope tag. Cells were collected for fixation in paraformaldehyde after 2 d of PAVE1 depletion and stained for epifluorescence microscopy. The localization pattern of TbAIR9 does not change after PAVE1 depletion. (E) Lysates were collected from control and PAVE1 RNAi cells in which TbAIR9 is endogenously tagged every 24 h during PAVE1 depletion and western blotted. TbAIR9 stability is not affected by PAVE1 depletion.

(TIF)

**S4 Fig. TbAIR9 depletion has differing effects on protein stability of array-associated proteins.** (A) Lysates were collected from control and TbAIR9 RNAi cells in which Tb927.9.10790 was endogenously tagged every 24 h during TbAIR9 depletion and western blotted. 10790-Ty1 protein levels decrease during TbAIR9 depletion. (B) Lysates were collected from control and TbAIR9 RNAi cells in which Tb927.11.1840 was endogenously tagged every 24 h during TbAIR9 depletion and western blotted. 1840-Ty1 protein levels are stable and increase during TbAIR9 depletion.

(TIF)

**S1 Table. Mass spectrometry analysis of mNG-PAVE1 immunoprecipitation.** Only proteins that were identified with a total unique peptide count of >5 were included for analysis.

(XLSX)

**S1 Movie. TIRF microscopy of 5 nM PAVE complex binding to Taxol-stabilized Cy5-labeled bovine microtubules.** Images were taken every 10 sec for 20 min. Movie is 10 frames per sec.

(MP4)

**S2 Movie. TIRF microscopy of 5 nM PAVE complex patches pre-seeded for 10 min on Taxol-stabilized Cy5-labeled bovine microtubules.** Unbound protein was washed out prior to imaging. Images were taken every 10 sec for 20 min. Movie is 10 frames per sec.

(MP4)

## Acknowledgments

The authors would like to thank Dr. Jeremy Balsbaugh (University of Connecticut Proteomics and Metabolomics Facility) for the mass spectrometry analysis. We would also like to thank

Geoff Williams (Brown University Leduc Bioimaging Facility) for helpful advice on our TEM preparations. We thank Dr. Sebastian Lourido (Massachusetts Institute of Technology) for the Ty1 antibody and Dr. Jack Sunter (Oxford Brookes University) for the TAT1 antibody. We thank Dr. Alexandra Deaconescu (Brown University) for the pOKD5 plasmid. We would like to thank TrypTag, whose data helped us identify Tb927.9.10790 and Tb927.11.1840. TrypTag is a data resource generated through a Wellcome Trust biomedical resource grant [108445/Z/15/Z] that was awarded to Prof. Keith Gull (University of Oxford), Prof. Mark Carrington (University of Cambridge), Prof. Christiane Hertz-Fowler (Wellcome Trust), Dr. Richard Wheeler (University of Oxford), Dr. Jack Sunter (Oxford Brookes University), Dr. Samuel Dean (University of Warwick) and Prof. Sue Vaughan (Oxford Brookes University). Work in C.L.d.G.'s laboratory is supported by the National Institutes of Health (F31AI143163 to A.N.S. and AI112953 to C.L.d.G.).

## Author Contributions

**Conceptualization:** Amy N. Sinclair, Christopher L. de Graffenried.

**Data curation:** Amy N. Sinclair, Christopher L. de Graffenried.

**Formal analysis:** Amy N. Sinclair, Christine T. Huynh, Christopher L. de Graffenried.

**Funding acquisition:** Amy N. Sinclair, Christopher L. de Graffenried.

**Investigation:** Amy N. Sinclair, Christine T. Huynh, Jenna L. Zuromski, Amanda E. Ruiz, Christopher L. de Graffenried.

**Methodology:** Amy N. Sinclair, Thomas E. Sladewski, Christopher L. de Graffenried.

**Project administration:** Christopher L. de Graffenried.

**Resources:** Christopher L. de Graffenried.

**Software:** Amy N. Sinclair.

**Supervision:** Christopher L. de Graffenried.

**Validation:** Amy N. Sinclair, Christopher L. de Graffenried.

**Visualization:** Amy N. Sinclair.

**Writing – original draft:** Amy N. Sinclair, Christopher L. de Graffenried.

**Writing – review & editing:** Amy N. Sinclair, Christine T. Huynh, Thomas E. Sladewski, Jenna L. Zuromski, Amanda E. Ruiz, Christopher L. de Graffenried.

## References

1. Fitzpatrick C, Nwankwo U, Lenk E, Vlas SJ de, Bundy DAP. An Investment Case for Ending Neglected Tropical Diseases. 3rd ed. Holmes KK, Bertozzi Stefano, Bloom Barry R, Jha P, editors. International Bank for Reconstruction and Development; 2017.
2. Vickerman K. The mechanism of cyclical development in trypanosomes of the *Trypanosoma brucei* subgroup: an hypothesis based on ultrastructural observations. *Transactions of the Royal Society of Tropical Medicine and Hygiene*. 1962; 56: 487–495. [https://doi.org/10.1016/0035-9203\(62\)90072-x](https://doi.org/10.1016/0035-9203(62)90072-x) PMID: 13997060
3. Angelopoulos E. Pellicular Microtubules in the Family Trypanosomatidae. *The Journal of Protozoology*. 1970; 17: 39–51. <https://doi.org/10.1111/j.1550-7408.1970.tb05157.x> PMID: 5420331
4. Sunter JD, Gull K. The Flagellum Attachment Zone: 'The Cellular Ruler' of Trypanosome Morphology. *Trends in parasitology*. 2016; 32: 309–324. <https://doi.org/10.1016/j.pt.2015.12.010> PMID: 26776656

5. Heddergott N, Krüger T, Babu SB, Wei A, Stellamanns E, Uppaluri S, et al. Trypanosome motion represents an adaptation to the crowded environment of the vertebrate bloodstream. Beverley SM, editor. *PLoS pathogens*. 2012; 8: e1003023. <https://doi.org/10.1371/journal.ppat.1003023> PMID: 23166495
6. Bargul JL, Jung J, McOdimba FA, Omogo CO, Adung'a VO, Krüger T, et al. Species-Specific Adaptations of Trypanosome Morphology and Motility to the Mammalian Host. Carrington M, editor. *PLoS pathogens*. 2016; 12: e1005448. <https://doi.org/10.1371/journal.ppat.1005448> PMID: 26871910
7. Sun SY, Kaelber JT, Chen M, Dong X, Nematbakhsh Y, Shi J, et al. Flagellum couples cell shape to motility in *Trypanosoma brucei*. *Proceedings of the National Academy of Sciences of the United States of America*. 2018; 115: E5916–E5925. <https://doi.org/10.1073/pnas.1722618115> PMID: 29891682
8. Capewell P, Cren-Travaillé C, Marchesi F, Johnston P, Clucas C, Benson RA, et al. The skin is a significant but overlooked anatomical reservoir for vector-borne African trypanosomes. *eLife*. 2016; 5: e17716. <https://doi.org/10.7554/eLife.17716> PMID: 27653219
9. Caljon G, Reet NV, Trez CD, Vermeersch M, Perez-Morga D, Abbeele JVD. The Dermis as a Delivery Site of *Trypanosoma brucei* for Tsetse Flies. Peters NC, editor. *PLoS pathogens*. 2016; 12: e1005744. <https://doi.org/10.1371/journal.ppat.1005744> PMID: 27441553
10. Trindade S, Rijo-Ferreira F, Carvalho T, Pinto-Neves D, Guegan F, Aresta-Branco F, et al. *Trypanosoma brucei* Parasites Occupy and Functionally Adapt to the Adipose Tissue in Mice. *Cell host & microbe*. 2016; 19: 837–848. <https://doi.org/10.1016/j.chom.2016.05.002> PMID: 27237364
11. Dóro É, Jacobs SH, Hammond FR, Schipper H, Pieters RP, Carrington M, et al. Visualizing trypanosomes in a vertebrate host reveals novel swimming behaviours, adaptations and attachment mechanisms. *eLife*. 2019; 8: 7140. <https://doi.org/10.7554/elife.48388> PMID: 31547905
12. Brooker BE. Fine structure of *Bodo saltans* and *Bodo caudatus* (Zoomastigophora: Protozoa) and their affinities with the Trypanosomatidae. *Bull Brit Mus Nat Hist*. 1971; 22: 89–102.
13. Robinson DR. Microtubule polarity and dynamics in the control of organelle positioning, segregation, and cytokinesis in the trypanosome cell cycle. *The Journal of Cell Biology*. 1995; 128: 1163–1172. <https://doi.org/10.1083/jcb.128.6.1163> PMID: 7896879
14. Sheriff O, Lim L-F, He CY. Tracking the biogenesis and inheritance of subpellicular microtubule in *Trypanosoma brucei* with inducible YFP- $\alpha$ -tubulin. *BioMed research international*. 2014; 2014: 1–12. <https://doi.org/10.1155/2014/893272> PMID: 24800253
15. Halliday C, Billington K, Wang Z, Madden R, Dean S, Sunter JD, et al. Cellular landmarks of *Trypanosoma brucei* and *Leishmania mexicana*. *Molecular and biochemical parasitology*. 2019; 230: 24–36. <https://doi.org/10.1016/j.molbiopara.2018.12.003> PMID: 30550896
16. Sherwin T, Gull K. Visualization of Detyrosination along Single Microtubules Reveals Novel Mechanisms of Assembly during Cytoskeletal Duplication in Trypanosomes. *Cell*. 1989; 57: 211–221. [https://doi.org/10.1016/0092-8674\(89\)90959-8](https://doi.org/10.1016/0092-8674(89)90959-8) PMID: 2649249
17. Bordier C, Garavito RM, Armbruster B. Biochemical and Structural Analyses of Microtubules in the Pellicular Membrane of *Leishmania tropica*. *Journal of Protozoology*. 1982; 29: 560–565. <https://doi.org/10.1111/j.1550-7408.1982.tb01335.x> PMID: 7175771
18. Souto-Padrón T, Souza W de, Heuser JE. Quick-freeze, deep-etch rotary replication of *Trypanosoma cruzi* and *Herpetomonas megaseliae*. *Journal of cell science*. 1984; 69: 167–178. PMID: 6386835
19. Meyer H, Souza W de. Electron Microscopic Study of *Trypanosoma cruzi* Periplast in Tissue Cultures. I. Number and Arrangement of the Peripheral Microtubules in the Various Forms of the Parasite's Life Cycle. *The Journal of Protozoology*. 1976; 23: 385–390. <https://doi.org/10.1111/j.1550-7408.1976.tb03792.x> PMID: 787513
20. Mitchison T, Kirschner M. Dynamic instability of microtubule growth. *Nature*. 1984; 312: 237–242. <https://doi.org/10.1038/312237a0> PMID: 6504138
21. Janke C. The tubulin code: molecular components, readout mechanisms, and functions. *The Journal of Cell Biology*. 2014; 206: 461–472. <https://doi.org/10.1083/jcb.201406055> PMID: 25135932
22. Rubinstein B, Larripa K, Sommi P, Mogilner A. The elasticity of motor-microtubule bundles and shape of the mitotic spindle. *Physical biology*. 2009; 6: 016005. <https://doi.org/10.1088/1478-3975/6/1/016005> PMID: 19193975
23. Sanchez T, Welch D, Nicastro D, Dogic Z. Cilia-like beating of active microtubule bundles. *Science*. 2011; 333: 456–459. <https://doi.org/10.1126/science.1203963> PMID: 21778400
24. Kwan AC, Dombeck DA, Webb WW. Polarized microtubule arrays in apical dendrites and axons. *Proceedings of the National Academy of Sciences of the United States of America*. 2008; 105: 11370–11375. <https://doi.org/10.1073/pnas.0805199105> PMID: 18682556
25. Forth S, Hsia K-C, Shimamoto Y, Kapoor TM. Asymmetric Friction of Nonmotor MAPs Can Lead to Their Directional Motion in Active Microtubule Networks. *Cell*. 2014; 157: 420–432. <https://doi.org/10.1016/j.cell.2014.02.018> PMID: 24725408

26. Janke C, Bulinski JC. Post-translational regulation of the microtubule cytoskeleton: mechanisms and functions. *Nature reviews Molecular cell biology*. 2011; 12: 773–786. <https://doi.org/10.1038/nrm3227> PMID: 22086369
27. Song Y, Brady ST. Post-translational modifications of tubulin: pathways to functional diversity of microtubules. *Trends in cell biology*. 2015; 25: 125–136. <https://doi.org/10.1016/j.tcb.2014.10.004> PMID: 25468068
28. Bechstedt S, Brouhard GJ. Doublecortin recognizes the 13-protofilament microtubule cooperatively and tracks microtubule ends. *Developmental cell*. 2012; 23: 181–192. <https://doi.org/10.1016/j.devcel.2012.05.006> PMID: 22727374
29. Reid TA, Coombes C, Mukherjee S, Goldblum RR, White K, Parmar S, et al. Structural state recognition facilitates tip tracking of EB1 at growing microtubule ends. *eLife*. 2019; 8: 6710. <https://doi.org/10.7554/eLife.48117> PMID: 31478831
30. Portran D, Zoccoler M, Gaillard J, Stoppin-Mellet V, Neumann E, Arnal I, et al. MAP65/Ase1 promote microtubule flexibility. *Molecular Biology of the Cell*. 2013; 24: 1964–1973. <https://doi.org/10.1091/mbc.E13-03-0141> PMID: 23615441
31. Sinclair AN, Graffenried CL de. More than Microtubules: The Structure and Function of the Subpellicular Array in Trypanosomatids. *Trends in parasitology*. 2019; 35: 760–777. <https://doi.org/10.1016/j.pt.2019.07.008> PMID: 31471215
32. Bramblett GT, Chang S, Flavin M. Periodic crosslinking of microtubules by cytoplasmic microtubule-associated and microtubule-corset proteins from a trypanosomatid. *Proceedings of the National Academy of Sciences*. 1987; 84: 3259–3263. <https://doi.org/10.1073/pnas.84.10.3259> PMID: 2883651
33. Balaban N, Waithaka HK, Njogu AR, Goldman R. Isolation of a subpellicular microtubule protein from *Trypanosoma brucei* that mediates crosslinking of microtubules. *Cell motility and the cytoskeleton*. 1989; 14: 393–400. <https://doi.org/10.1002/cm.970140309> PMID: 2582498
34. Vedrenne C, Giroud C, Robinson DR, Besteiro S, Bosc C, Bringaud F, et al. Two related subpellicular cytoskeleton-associated proteins in *Trypanosoma brucei* stabilize microtubules. Goldstein LS, editor. *Molecular Biology of the Cell*. 2002; 13: 1058–1070. <https://doi.org/10.1091/mbc.01-06-0298> PMID: 11907282
35. May SF, Peacock L, Costa CICA, Gibson WC, Tetley L, Robinson DR, et al. The *Trypanosoma brucei* AIR9-like protein is cytoskeleton-associated and is required for nucleus positioning and accurate cleavage furrow placement. *Molecular microbiology*. 2012; 84: 77–92. <https://doi.org/10.1111/j.1365-2958.2012.08008.x> PMID: 22329999
36. Baines A, Gull K. WCB is a C2 domain protein defining the plasma membrane—sub-pellicular microtubule corset of kinetoplastid parasites. *Protist*. 2008; 159: 115–125. <https://doi.org/10.1016/j.protis.2007.09.001> PMID: 17951107
37. Olego-Fernandez S, Vaughan S, Shaw MK, Gull K, Ginger ML. Cell morphogenesis of *Trypanosoma brucei* requires the paralogous, differentially expressed calpain-related proteins CAP5.5 and CAP5.5V. *Protist*. 2009; 160: 576–590. <https://doi.org/10.1016/j.protis.2009.05.003> PMID: 19656721
38. Portman N, Gull K. Identification of paralogous life-cycle stage specific cytoskeletal proteins in the parasite *Trypanosoma brucei*. Li Z, editor. *PloS one*. 2014; 9: e106777. <https://doi.org/10.1371/journal.pone.0106777> PMID: 25180513
39. Sherwin T, Gull K. The cell division cycle of *Trypanosoma brucei brucei*: timing of event markers and cytoskeletal modulations. *Philosophical Transactions of the Royal Society B: Biological Sciences*. 1989; 323: 573–588. <https://doi.org/10.1098/rstb.1989.0037> PMID: 2568647
40. Wheeler RJ, Scheumann N, Wickstead B, Gull K, Vaughan S. Cytokinesis in *Trypanosoma brucei* differs between bloodstream and tsetse trypomastigote forms: implications for microtubule-based morphogenesis and mutant analysis. *Molecular microbiology*. 2013; 90: 1339–1355. <https://doi.org/10.1111/mmi.12436> PMID: 24164479
41. Abeywickrema M, Vachova H, Farr H, Mohr T, Wheeler RJ, Lai D-H, et al. Non-equivalence in old- and new-flagellum daughter cells of a proliferative division in *Trypanosoma brucei*. *Molecular microbiology*. 2019; 112: 1024–1040. <https://doi.org/10.1111/mmi.14345> PMID: 31286583
42. Wheeler RJ, Gull K, Sunter JD. Coordination of the Cell Cycle in Trypanosomes. *Annual Review of Microbiology*. 2019; 73: 133–154. <https://doi.org/10.1146/annurev-micro-020518-115617> PMID: 31500537
43. Hilton NA, Sladewski TE, Perry JA, Pataki Z, Sinclair-Davis AN, Muniz RS, et al. Identification of TOE-FAZ1-interacting proteins reveals key regulators of *Trypanosoma brucei* cytokinesis. *Molecular microbiology*. 2018; 109: 306–326. <https://doi.org/10.1111/mmi.13986> PMID: 29781112
44. Wehland J, Willingham M, Sandoval I. A rat monoclonal antibody reacting specifically with the tyrosylated form of alpha-tubulin. I. Biochemical characterization, effects on microtubule polymerization in

- vitro, and microtubule polymerization and organization in vivo. *The Journal of Cell Biology*. 1983; 97: 1467–1475. <https://doi.org/10.1083/jcb.97.5.1467> PMID: 6415068
45. Sherwin T, Schneider A, Sasse R, Seebeck T, Gull K. Distinct localization and cell cycle dependence of COOH terminally tyrosinolated alpha-tubulin in the microtubules of *Trypanosoma brucei brucei*. *The Journal of Cell Biology*. 1987; 104: 439–446. <https://doi.org/10.1083/jcb.104.3.439> PMID: 3546334
  46. Stephan A, Vaughan S, Shaw MK, Gull K, McKean PG. An Essential Quality Control Mechanism at the Eukaryotic Basal Body Prior to Intraflagellar Transport. *Traffic*. 2007; 8: 1323–1330. <https://doi.org/10.1111/j.1600-0854.2007.00611.x> PMID: 17645436
  47. Woods A, Sherwin T, Sasse R, MacRae TH, Baines AJ, Gull K. Definition of individual components within the cytoskeleton of *Trypanosoma brucei* by a library of monoclonal antibodies. *Journal of cell science*. 1989; 93: 491–500. PMID: 2606940
  48. Schindelin J, Arganda-Carreras I, Frise E, Kaynig V, Longair M, Pietzsch T, et al. Fiji: an open-source platform for biological-image analysis. *Nat Methods*. 2012; 9: 676–682. <https://doi.org/10.1038/nmeth.2019> PMID: 22743772
  49. Griffiths G, Lucocq JM. Antibodies for immunolabeling by light and electron microscopy: not for the faint hearted. *Histochem Cell Biol*. 2014; 142: 347–360. <https://doi.org/10.1007/s00418-014-1263-5> PMID: 25151300
  50. Los GV, Encell LP, McDougall MG, Hartzell DD, Karassina N, Zimprich C, et al. HaloTag: a novel protein labeling technology for cell imaging and protein analysis. *ACS chemical biology*. 2008; 3: 373–382. <https://doi.org/10.1021/cb800025k> PMID: 18533659
  51. Kelley LA, Mezulis S, Yates CM, Wass MN, Sternberg MJE. The Phyre2 web portal for protein modeling, prediction and analysis. *Nat Protoc*. 2015; 10: 845–858. <https://doi.org/10.1038/nprot.2015.053> PMID: 25950237
  52. Raman S, Vernon R, Thompson J, Tyka M, Sadreyev R, Pei J, et al. Structure prediction for CASP8 with all-atom refinement using Rosetta. *Proteins Struct Funct Bioinform*. 2009; 77: 89–99. <https://doi.org/10.1002/prot.22540> PMID: 19701941
  53. Blum M, Chang H-Y, Chuguransky S, Grego T, Kandasaamy S, Mitchell A, et al. The InterPro protein families and domains database: 20 years on. *Nucleic Acids Res*. 2020;49. <https://doi.org/10.1093/nar/gkaa977> PMID: 33156333
  54. Buchan DWA, Jones DT. The PSIPRED Protein Analysis Workbench: 20 years on. *Nucleic Acids Res*. 2019; 47: W402–W407. <https://doi.org/10.1093/nar/gkz297> PMID: 31251384
  55. Jaroszewski L, Li Z, Cai X, Weber C, Godzik A. FFAS server: novel features and applications. *Nucleic acids research*. 2011; 39: W38–44. <https://doi.org/10.1093/nar/gkr441> PMID: 21715387
  56. Finn RD, Clements J, Eddy SR. HMMER web server: interactive sequence similarity searching. *Nucleic Acids Res*. 2011; 39: W29–W37. <https://doi.org/10.1093/nar/gkr367> PMID: 21593126
  57. Altschul SF, Madden TL, Schäffer AA, Zhang J, Zhang Z, Miller W, et al. Gapped BLAST and PSI-BLAST: a new generation of protein database search programs. *Nucleic Acids Res*. 1997; 25: 3389–3402. <https://doi.org/10.1093/nar/25.17.3389> PMID: 9254694
  58. Lupas A, Dyke MV, Stock J. Predicting coiled coils from protein sequences. *Science*. 1991; 252: 1162–1164. <https://doi.org/10.1126/science.252.5009.1162> PMID: 2031185
  59. Maccioni RB, Cambiasso V. Role of microtubule-associated proteins in the control of microtubule assembly. *Physiol Rev*. 1995; 75: 835–864. <https://doi.org/10.1152/physrev.1995.75.4.835> PMID: 7480164
  60. Goodson HV, Jonasson EM. Microtubules and Microtubule-Associated Proteins. *Csh Perspect Biol*. 2018; 10: a022608. <https://doi.org/10.1101/cshperspect.a022608> PMID: 29858272
  61. Rodionov VI, Gyoeva FK, Kashina AS, Kuznetsov SA, Gelfand VI. Microtubule-associated proteins and microtubule-based translocators have different binding sites on tubulin molecule. *The Journal of Biological Chemistry*. 1990; 265: 5702–5707. PMID: 2138610
  62. Buschmann H, Chan J, Sanchez-Pulido L, Andrade-Navarro MA, Doonan JH, Lloyd CW. Microtubule-associated AIR9 recognizes the cortical division site at preprophase and cell-plate insertion. *Current Biology*. 2006; 16: 1938–1943. <https://doi.org/10.1016/j.cub.2006.08.028> PMID: 17027491
  63. Dean S, Sunter JD, Wheeler RJ. TrypTag.org: A Trypanosome Genome-wide Protein Localisation Resource. *Trends in parasitology*. 2017; 33: 80–82. <https://doi.org/10.1016/j.pt.2016.10.009> PMID: 27863903
  64. Aslett M, Aurrecochea C, Berriman M, Brestelli J, Brunk BP, Carrington M, et al. TriTrypDB: a functional genomic resource for the Trypanosomatidae. *Nucleic acids research*. 2010; 38: D457–62. <https://doi.org/10.1093/nar/gkp851> PMID: 19843604
  65. Mészáros B, Erdős G, Dosztányi Z. IUPred2A: context-dependent prediction of protein disorder as a function of redox state and protein binding. *Nucleic Acids Res*. 2018;46. <https://doi.org/10.1093/nar/gky384> PMID: 29860432

66. Tran JQ, Li C, Chyan A, Chung L, Morrissette NS. SPM1 Stabilizes Subpellicular Microtubules in *Toxoplasma gondii*. *Eukaryot Cell*. 2012; 11: 206–216. <https://doi.org/10.1128/EC.05161-11> PMID: 22021240
67. Harding CR, Gow M, Kang JH, Shortt E, Manalis SR, Meissner M, et al. Alveolar proteins stabilize cortical microtubules in *Toxoplasma gondii*. *Nat Commun*. 2019; 10: 401. <https://doi.org/10.1038/s41467-019-08318-7> PMID: 30674885
68. Harding CR, Frischknecht F. The Riveting Cellular Structures of Apicomplexan Parasites. *Trends Parasitol*. 2020; 36: 979–991. <https://doi.org/10.1016/j.pt.2020.09.001> PMID: 33011071
69. Engstler M, Pfohl T, Herminghaus S, Boshart M, Wiegertjes G, Heddergott N, et al. Hydrodynamic flow-mediated protein sorting on the cell surface of trypanosomes. *Cell*. 2007; 131: 505–515. <https://doi.org/10.1016/j.cell.2007.08.046> PMID: 17981118
70. Krüger T, Schuster S, Engstler M. Beyond Blood: African Trypanosomes on the Move. *Trends in parasitology*. 2018; 34: 1056–1067. <https://doi.org/10.1016/j.pt.2018.08.002> PMID: 30181072
71. Cannon KS, Woods BL, Crutchley JM, Gladfelter AS. An amphipathic helix enables septins to sense micrometer-scale membrane curvature. *J Cell Biol*. 2019; 218: 1128–1137. <https://doi.org/10.1083/jcb.201807211> PMID: 30659102
72. Woods A, Baines AJ, Gull K. A high molecular mass phosphoprotein defined by a novel monoclonal antibody is closely associated with the intermicrotubule cross bridges in the *Trypanosoma brucei* cytoskeleton. *Journal of cell science*. 1992; 103: 665–675. PMID: 1478963
73. Hemphill A, Seebeck T, Lawson D. The *Trypanosoma brucei* Cytoskeleton: Ultrastructure and Localization of Microtubule-Associated and Spectrin-like Proteins Using Quick-Freeze, Deep-Etch, Immunogold Electron Microscopy. *Journal of structural biology*. 1991; 107: 211–220. [https://doi.org/10.1016/1047-8477\(91\)90046-y](https://doi.org/10.1016/1047-8477(91)90046-y) PMID: 1725491
74. Bechstedt S, Lu K, Brouhard GJ. Doublecortin Recognizes the Longitudinal Curvature of the Microtubule End and Lattice. *Current Biology*. 2014; 24: 2366–2375. <https://doi.org/10.1016/j.cub.2014.08.039> PMID: 25283777
75. Chrétien D, Fuller SD, Karsenti E. Structure of growing microtubule ends: two-dimensional sheets close into tubes at variable rates. *Journal of Cell Biology*. 1995; 129: 1311–1328. <https://doi.org/10.1083/jcb.129.5.1311> PMID: 7775577
76. Benz C, Clucas C, Mottram JC, Hammarton TC. Cytokinesis in bloodstream stage *Trypanosoma brucei* requires a family of katanins and spastin. Zilberstein D, editor. *PloS one*. 2012; 7: e30367. <https://doi.org/10.1371/journal.pone.0030367> PMID: 22279588
77. Zhou Q, An T, Pham KTM, Hu H, Li Z. The C1F1 protein is a master orchestrator of trypanosome cytokinesis that recruits several cytokinesis regulators to the cytokinesis-initiation site. *The Journal of Biological Chemistry*. 2018; 293: 16177–16192. <https://doi.org/10.1074/jbc.RA118.004888> PMID: 30171070
78. Hu L, Hu H, Li Z. A kinetoplastid-specific kinesin is required for cytokinesis and for maintenance of cell morphology in *Trypanosoma brucei*. *Molecular microbiology*. 2012; 83: 565–578. <https://doi.org/10.1111/j.1365-2958.2011.07951.x> PMID: 22168367
79. Hu H, Hu L, Yu Z, Chasse AE, Chu F, Li Z. An orphan kinesin in trypanosomes cooperates with a kinetoplastid-specific kinesin to maintain cell morphology by regulating subpellicular microtubules. *Journal of cell science*. 2012; 125: 4126–4136. <https://doi.org/10.1242/jcs.106534> PMID: 22623724
80. de Graffenried CL, Anrather D, Raubendorf Von F, Warren G. Polo-like kinase phosphorylation of bilobe-resident TbCentrin2 facilitates flagellar inheritance in *Trypanosoma brucei*. *Mol Biol Cell*. 2013 Jun; 24(12):1947–63. <https://doi.org/10.1091/mbc.E12-12-0911> PMID: 23615446
81. Wirtz E. A tightly regulated inducible expression system for conditional gene knock-outs and dominant-negative genetics in *Trypanosoma brucei*. *Molecular and biochemical parasitology*. 1999; 1–13. [https://doi.org/10.1016/s0166-6851\(99\)00002-x](https://doi.org/10.1016/s0166-6851(99)00002-x) PMID: 10215027
82. McAllaster MR, Sinclair-Davis AN, Hilton NA, Graffenried CL de. A unified approach towards *Trypanosoma brucei* functional genomics using Gibson assembly. *Molecular and biochemical parasitology*. 2016; 210: 13–21. <https://doi.org/10.1016/j.molbiopara.2016.08.001> PMID: 27496178
83. Redmond S, Vadivelu J, Field MC. RNAi: an automated web-based tool for the selection of RNAi targets in *Trypanosoma brucei*. *Molecular and biochemical parasitology*. 2003; 128: 115–118. [https://doi.org/10.1016/s0166-6851\(03\)00045-8](https://doi.org/10.1016/s0166-6851(03)00045-8) PMID: 12706807
84. Shaner NC, Lambert GG, Chammas A, Ni Y, Cranfill PJ, Baird MA, et al. A bright monomeric green fluorescent protein derived from *Branchiostoma lanceolatum*. *Nature methods*. 2013; 10: 407–409. <https://doi.org/10.1038/nmeth.2413> PMID: 23524392
85. Cox J, Mann M. MaxQuant enables high peptide identification rates, individualized p.p.b.-range mass accuracies and proteome-wide protein quantification. *Nature biotechnology*. 2008; 26: 1367–1372. <https://doi.org/10.1038/nbt.1511> PMID: 19029910

86. Schmidt TGM, Skerra A. The Strep-tag system for one-step purification and high-affinity detection or capturing of proteins. *Nature Protocols*. 2007; 2: 1528–1535. <https://doi.org/10.1038/nprot.2007.209> PMID: [17571060](https://pubmed.ncbi.nlm.nih.gov/17571060/)
87. Sladewski TE, Billington N, Ali MY, Bookwalter CS, Lu H, Kremmentsova EB, et al. Recruitment of two dyneins to an mRNA-dependent Bicaudal D transport complex. *eLife*. 2018; 7: 1169. <https://doi.org/10.7554/eLife.36306> PMID: [29944116](https://pubmed.ncbi.nlm.nih.gov/29944116/)
88. Schmidt-Cernohorska M, Zhernov I, Steib E, Guennec ML, Achek R, Borgers S, et al. Flagellar microtubule doublet assembly in vitro reveals a regulatory role of tubulin C-terminal tails. *Science*. 2019; 363: 285–288. <https://doi.org/10.1126/science.aav2567> PMID: [30655442](https://pubmed.ncbi.nlm.nih.gov/30655442/)
89. Lord SJ, Velle KB, Mullins RD, Fritz-Laylin LK. SuperPlots: Communicating reproducibility and variability in cell biology. *Journal of Cell Biology*. 2020; 219: 94. <https://doi.org/10.1083/jcb.202001064> PMID: [32346721](https://pubmed.ncbi.nlm.nih.gov/32346721/)